DOI: https://dx.doi.org/10.4314/gjgs.v22i1.7

GLOBAL JOURNAL OF GEOLOGICAL SCIENCES VOL. 22, 2024: 79-112
COPYRIGHT© BACHUDO SCIENCE CO. LTD PRINTED IN NIGERIA ISSN 1596-6798, e-ISSN: 2992–4502
www.globaljournalseries.com.ng, Email: globaljournalseries@gmail.com



# GEOCHEMISTRY OF AWI SANDSTONE, CALABAR FLANK, SOUTHEASTERN (SE) NIGERIA: CONSTRAINTS ON THE METAL ENRICHMENT, PROVENANCE, AND TECTONIC SETTING

**TEMPLE OKAH ARIKPO, MOROD IWONG MORPHY, GODWIN AMAH, BENJAMIN ODEY OMANG AND OJIKUTU LATIFA TIJANI**

(Received 14 June 2024; Revision Accepted 17 July 2024)

## ABSTRACT

As the global population continues to rise, the search for crucial metals has become a primary concern for mineral explorers due to their non-renewable nature. To keep pace with increasing need for solid mineral exploration and exploitation, it is then important to find new deposits and engage in sustainable extraction practices. The aim of the study is to analyze the geochemical composition of Awi sandstone, focusing on metal enrichment, origin, and the tectonic setting of the protolith. For this purpose, fifteen (15) fresh samples from the Awi sandstones were collected for geochemical analysis using inductively coupled plasma mass spectrometry (ICP-MS). Results indicate that Ba, Rb, Sr, Cr, Zn, Ni, Y, and Cu are present in higher concentrations while As, Be, Bi, Cd, Hf, Hg, Mo, Sc, U, and Pb are depleted. The findings also suggest an increase in abundance of LREE and a decrease in availability of HREE. The $TiO_2$ versus Zr discrimination diagram with the primary element suggests that the parent rock of Awi sandstone was mainly of intermediate-felsic igneous origin. The classification plot of $Na_2O$+$K_2O$ to $SiO_2$, and the R1-R2 plot, indicate that the majority of Awi sandstones originated from granodiorite protolith. The plots comparing Th/Yb to Ta/Yb, Th/Ta to Yb, and ($K_2O$/$Na_2O$) to $SiO_2$ suggest that these Awi sandstones were formed in a passive to active continental margin environment. So which of the elements listed may probably denote crucial ore deposit.

**KEYWORDS:** Geochemistry – Awi Sandstones – Calabar Flank – Metal enrichment

## INTRODUCTION

Geochemical analysis is an advanced analytical technique used to decipher origin of the sediments, the tectonic conditions during deposition, and assess potential metal concentration in rocks. Thus, it is essential to conduct a geochemical analysis of the Awi Sandstone in the Calabar Flank. The Calabar Flank, located in southeastern Nigeria, is a prominent sedimentary basin (Ekpo et al., 2012; Boboye and Okon, 2014); surrounded by the Oban Massif to the north, the Niger Delta to the south, the Cameroon volcanic ridge to the east, and the Ikpe platform to the west.

The oldest geological unit in this basin is the Awi Formation, which consists of mudstones, conglomerates, and sandstones (Ekwok et al., 2020). The Awi Sandstone consists mainly of sand-sized (0.0625 to 2 mm) silicate grains, with quartz being the predominant mineral due to its high resistance to weathering (Goswami and Deopa, 2018; Garzanti, 2019). The mineral composition of sandstones plays a significant role in determining the types and quantities of minerals that can be deposited. For instance, sandstones rich in feldspar are more susceptible to alteration by hydrothermal fluids, which can introduce valuable minerals such as gold, silver, and copper (Bogossian et al., 2020).

**Temple Okah Arikpo,** Department of Geology, University of Calabar, Calabar, Nigeria
**Morod Iwong Morphy,** Department of Geology, University of Calabar, Calabar, Nigeria
**Godwin Amah,** Department of Geology, University of Calabar, Calabar, Nigeria
**Benjamin Odey Omang,** Department of Geology, University of Calabar, Calabar, Nigeria
**Ojikutu Latifa Tijani,** Department of Geology, University of Calabar, Calabar, Nigeria

Sandstones exhibit notable porosity and permeability, facilitating the deposition of minerals within the rock's pores (Shu et al., 2021; Wang et al., 2022). The deposition of minerals is also impacted by the mineral composition of the surrounding rocks and fluids, with elements like sulfur promoting the formation of sulfide minerals such as pyrite and chalcopyrite (Huston et al.,1995; Tornos, 2006; Misra, 2012; Revan et al., 2014).

Extensive research and documentation have been conducted on base metal deposits in sandstone found in sediments of various geological ages (Samama 1976; Fleischer 1984; Hayes and Einaudi 1986; Bjørlykke et al., 2019). In the sandstones of the Newland Formation, there is a distinct series of minerals produced through diagenetic processes, including pyrite, sphalerite, galena, chalcopyrite, silica, dolomite, and calcite (Fleischer, 1984). The pore spaces between detrital grains in these sandstones are predominantly occupied by sphalerite and galena (Schieber, 1991; White et al., 2014). Sphalerite forms on the surfaces of quartz grains early in the diagenetic process, while galena develops at a later stage, filling remaining pore spaces and often growing over existing sphalerite cement (Oyebamiji et al., 2023; Rickard et al., 1979).

Pb-Zn mineralization in the Newland Formation resembles the dispersed sulfide deposits in sandstone-hosted lead deposits and the Revett Quartzite of the Coeur d'Alene district (Samama, 1976; Bjørlykke et al., 2019). This mineralization style is prevalent in the Belt Series Formation. Disseminated base metal deposits in the Belt Series are commonly situated beneath a sediment layer of at least 9 km. In Australia, sediment accumulations underlying stratiform Pb-Zn deposits extend for over 3 km and serve as the primary source of ore metals. The presence of thicker sediment piles can impact the availability of metal content for the formation of deposits. Thicker basin fills are associated with higher temperatures that influence the release of metals during the transformation of smectite to illite, increased solubility of base metals in basin fluids, and the potential for intermittent fluid removal.

In a study conducted by Spears (1987) on Triassic sandstones in the West Midlands of England, it was found that elements such as Zn, Pb, Cu, Cr, Ni, and Sr were enriched at shallow depths (less than 1 m). Another investigation by Zaid (2015) on the geochemistry of Pliocene Gabir Formation sandstones in North Marsa Alam, Red Sea, Egypt, revealed an enrichment of trace elements such as Barium (Ba), Strontium (Sr), Nickel (Ni), Chromium (Cr), and Zircon (Zr), as well as a decrease in Uranium (U) and Thorium (Th). The geochemical analysis indicates that the deposition occurred in a basin along an active continental margin, mainly sourced from granitic and low-grade metamorphic materials. The protoliths, which include Proterozoic granites, meta-gabbros, and metavolcanics, were exposed by Oligocene rifting and continued post-Miocene.

The Ajali Sandstone, located in the Anambra Basin in southeastern Nigeria, is a prominent geological formation characterized by coarse-grained, well-sorted sandstone with cross-bedding features. This sandstone is known for its significant concentration of heavy minerals, including zircon, rutile, ilmenite, and tourmaline, which are often concentrated in specific horizons and can be economically viable for extraction. Additionally, the Ajali Sandstone contains high-purity silica sand, making it suitable for the glass-making industry due to its high quartz content and well-rounded grains (Ogbahon and Opeloye, 2016). In the Upper Benue Trough, the Bima Sandstone is a significant Cretaceous formation consisting of thick sequences of arkosic sandstones and conglomerates. It primarily represents a fluvial deposit with some sections indicating shallow marine influence. The Bima Sandstone is notable for its potential uranium mineralization, particularly in its basal sections, where deposits are associated with reduction zones rich in organic matter. There are also occurrences of barite mineralization, especially in areas where the formation has undergone structural deformation, such as faulting and fracturing. Barite is an important industrial mineral used in the oil and gas industry as a weighting agent in drilling muds (Olade, 2020). The Gongila Sandstone, part of the Gongola Basin in northeastern Nigeria, comprises mainly sandstone with interbedded siltstone and shale, deposited in a transitional marine environment. It has been reported to contain phosphatic nodules, indicating potential for phosphate mining, which is critical for producing fertilizers and various industrial chemicals. The Gongila Sandstone also serves as a reservoir rock in the Gongola Basin, with its porosity and permeability making it a suitable target for hydrocarbon exploration. The sandstone is known to contain oil and gas, particularly where it is capped by impermeable shale formations (Adekoya et al., 2014).

Despite extensive research efforts, it is crucial to conduct a geochemical assessment of the Awi Sandstone in the Calabar Flank to better understand sediment provenance, tectonic setting, and the potential for metal enrichment. Geochemical studies in the Calabar Flank, Nigeria, have focused on assessing hydrocarbon potential, characterizing sediments, evaluating environmental impacts, and understanding the petrogenesis of sandstones. The objective of this study is to analyze the geochemistry of the Awi Sandstones in the Calabar Flank, utilizing variation plots, bivariate plots, and spider diagrams, in order to determine sediment provenance, tectonic context, and metal enrichment potential.

**Location of the Study Area**

The focus of the research is the Calabar Flank in southeastern Nigeria, situated between latitude 5°0'0"N and 5°15'0"N, and longitude 8°15'0"E to 8°30'0"E (Figure 1). A region of great geological significance, the Calabar Flank in southeastern Nigeria covers a vast area of land.

**Geology and Tectonic Setting**

The Awi Sandstone, of the Calabar Flank of southeastern Nigeria, is a member of the Awi Formation and represents the earliest sedimentary deposit in the region (Figure 2). It comprises mainly of immature arkosic sandstones and conglomerates, with some mudstone, shales, and carbonaceous elements, as well as exhibits cyclical fining-upward patterns (Nton, 1999). With a thickness of approximately 50 m, the Awi Formation overlays Basement Complex which is primarily made up of banded amphibolites (Macaulay et al., 2016).

The Calabar Flank s a coastal sedimentary basin that formed during the Early Cretaceous rifting period. During the early Cretaceous period, the stretching of the Earth's crust caused sinking along significant fault lines, especially the inland extensions of the Chain and Charcot fault systems. This resulted in the formation of the Benue Trough, which is an unsuccessful extension of the RRR triple junction.

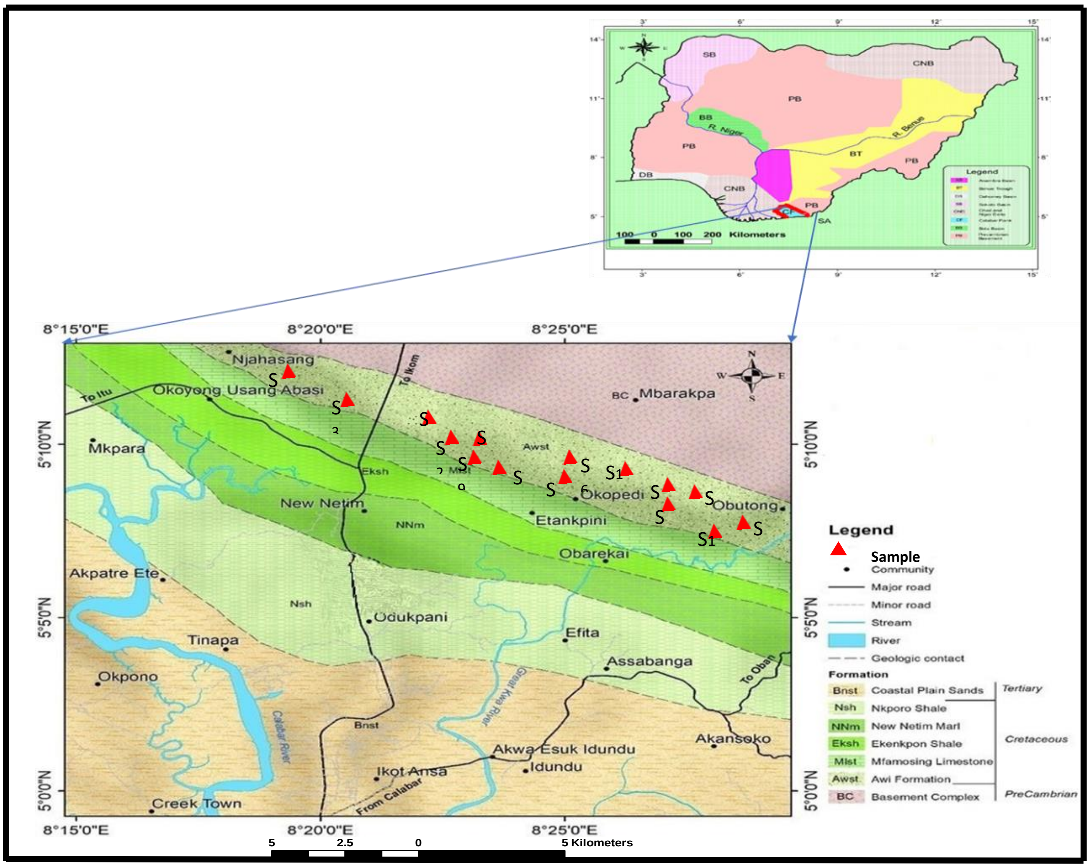


FIG. 1: Location of the Study Area

| AGE | LITHOLOGY | | DESCRIPTION |
|---|---|---|---|
| Recent Eocene - | Benin Formation | | Loose sands, pebbly and arkosic |
| Maastrichtian L. Campanian - | Nkporo Shale | | Dark grey, very fissile carbonaceous shale with gypsum bands and some calcareous nodules |
| Santonian | Santonian Deformation | | Santonian deformational episode characterized by period of folding of pre-existing rocks and erosion and/or non deposition. |
| Coniacian | ODUKPANI GROUP | New Netim Marl | Dark grey massive marls intercalating with flaggy, calcareous grey shale with thalassinoides structures |
| Turonian | ODUKPANI GROUP | Ekenkpon Shale | Grey fissile shale with thin bands of calcareous nodules, limestone and mudstone units. Abundant shell fragments, keeled ammonite, juvenile |
| Cenomanian | ODUKPANI GROUP | Un-named Shale | Dark gray shale, highly fissile and separated by the upper shale unit by a regressive mudstone |
| Mid - Albian | ODUKPANI GROUP | Mfamosing Limestone | White to light grey limestone, stromatolitic at the base, with abundant fossils (gastropods, corals, shell fragments) |
| Neocomian - Aptian | Awi Formation | | Reddish brown, coarse to medium grained arkosic sandstone. Pebbly at the base and exhibit fining upward succession in cycles, graded bedding. |
| Precambrian | Precambrian Basement Complex | | Southeastern Basement Complex – Oban Massif composed predominantly of granite gneisses, granites and granodiorites. |

FIG. 2. Stratigraphic chart of the Calabar Flank (Modified after Boboye and Okon, 2014)

The Charcot fault system acts as a boundary between the Niger Delta Basin and the Calabar Flank (Eldosouky et al., 2022; Ekpo et al., 2013; Opara et al., 2014) (Figure 3).

The rock layers of the Calabar Flank mainly date back to the Cretaceous period (Figure 2). In certain areas close to Calabar, Cretaceous sediments lie beneath layers from the Cenozoic Benin Formation (from the Paleogene to Neogene periods) and more recent formations from the Niger Delta (Boboye and Okon, 2014). The structural orientations in the region follow a northwest-southeast direction and have been influenced by uplifted blocks and depressed areas formed through faulting in the Earth's crust. The deposition of sediment in the basin commenced with the Awi Formation's Neocomian-Aptian fluvial sandstones, which formed during the initial phase of the rift (Boboye and Okon, 2014). Subsequently, post-rift marine deposits of the Albian and Late Cretaceous Odukpani Group, including the Mfamosing Limestone of the mid-Albian age, the Ekenkpon Formation of the Late Albian-Turonian age, and the New Netim Marl of the Coniacian age, were established. These marine sediments developed directly above the Awi Formation during a period of rising relative sea levels. The Nkporo Shale, dating back to the Late Campanian-Maastrichtian period, is irregularly positioned on top of the Odukpani Group. The Benin Formation, comprising Palaeogene and more recent regressive sands and gravel beds, overlays these Cretaceous strata (Edet and Nyong, 1994).

## MATERIALS AND METHODS

### Materials

The study utilized the following field materials: Global Positioning System (GPS), compass, hand auger, sample bags, masking tape, and a marker pen. The laboratory was equipped with mortar and pestle, sieve, weighing balance, and pharmaceutical bag

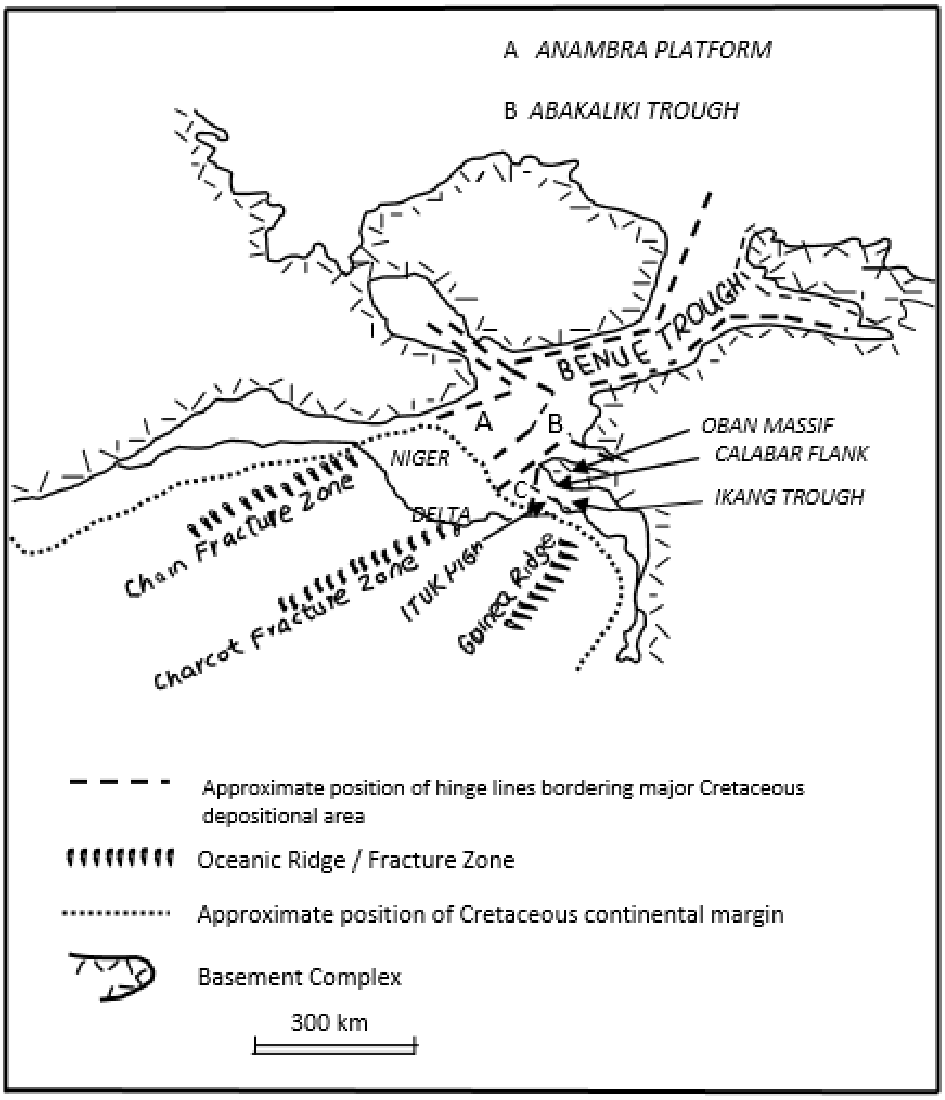


FIG. 3. Structural Framework of the Calabar Flank and adjacent areas (Odumodu et al., 2012)

**Methods**

Extensive fieldwork was conducted to gather fresh sand samples from various outcrops within the Awi Formation, totaling fifteen samples weighing between 30 and 50 kg. The sandstones' variable exposure necessitated collecting the samples at random from a depth of around 1 m. After air-drying for two weeks, the samples were crushed and sieved through a 10-mesh screen with a particle size less than 2 mm at the Department of Geology laboratory, University of Calabar, Calabar. The powdered samples, each weighing 30 g, were sealed in pharmaceutical containers before being sent to the Activation Laboratories (Act Lab) in Canada for geochemical analysis. The concentrations of major, minor, and trace elements were determined using Inductively Coupled Plasma-Mass Spectrometry (ICP-MS).

**Data interpretation**

Statistical analysis of the data was conducted using Microsoft Excel 2016, and GCDkit software was utilized to create discrimination plots. Excel software was used to generate scattered plots illustrating the metal enrichment and depletion. To gain insights into the nature of the source rocks (protolith) of the Awi sandstones, various discrimination plots, such as $TiO_2$ versus Zr (Hayashi et al., 1997) and Discriminant Function 1 versus Discriminant Function 2 diagram for provenance (Murali et al., 1983), Th/Yb versus Zr/Y (Ross and Bedard, 2009), FeOt/MgO versus $SiO_2$ (Miyashiro 1974), AFM ternary plot (Irvine and Baragar, 1971), $SiO_2$ versus $K_2O$ discrimination plot (Peccerillo and Taylor 1976), Co versus Th plot (Hastie et al., 2007), plot of $(Al_2O_3+CaO)/(FeOt+Na_2O+K_2O)$ versus $100(MgO+FeOt+TiO_2)/SiO_2$ (Sylvester, 1989), Molar $Na_2O$-$Al_2O_3$-$K_2O$ plot (Salisu et al., 2022), B(Fe+Mg+Ti) versus A(K+Na+2Ca), discrimination plot (modified by Villaseca et al., 1998), A/CNK versus A/NK diagram (After Shand 1943), QAPF diagram – Si oversaturated for intrusive igneous rocks, $Na_2O$+$K_2O$ vs $SiO_2$ classification plot of plutonic igneous rocks (Cox, 2013), $Na_2O$+$K_2O$ vs $SiO_2$ plot (Middlemost, 1985), $Na_2O$+$K_2O$ vs $SiO_2$ plot (Middlemost, 1994), and R1-R2 classification plot for plutonic igneous rocks (De la Roche et al., 1980) were used. To understand the tectonic setting of the study area, varied discrimination plots were employed. These plots include; The Y+Nb versus Rb tectonic discrimination plot (Pearce et al., 1984), Y versus Nb tectonic discrimination diagram (Pearce et al., 1984), Zr versus Nb/Zr, Nb/Yb versus Th/Yb (Pearce 2008), and tectonic discrimination diagram of $K_2O/Na_2O$ versus $TiO_2$.by Roser and Korsch (1988).

## RESULTS AND DISCUSSION

The results of geochemical analysis of the sandstones analyzed are presented in Tables 1 - 2.

### Major Oxide Geochemistry

The data in Table 1 indicates that the Awi sandstone samples exhibit high levels of silicon dioxide ($SiO_2$) and aluminum oxide ($Al_2O_3$). The $SiO_2$ content typically falls within the range of 60% to 80%, while $Al_2O_3$ levels range from 13% to 17%, indicating a significant presence of quartz and feldspar, which are abundant minerals in sandstone. Additionally, the analysis revealed lower quantities of iron oxide ($Fe_2O_3$), magnesium oxide (MgO), calcium oxide (CaO), and sodium oxide ($Na_2O$) in comparison to certain reference materials. Normally, $Fe_2O_3$ content is below 10%, while the levels of MgO, CaO, and $Na_2O$ range between 0.5% to 1.5%, 1% to 2%, and around 1%, respectively. The presence of iron oxides, pyroxenes, calcite, or Na-feldspar in Awi sandstone is quite minimal compared to other rock types like basalt, gabbro, granite, and diorite. The potassium oxide ($K_2O$) content ranges from 1% to 5%, indicating the possible existence of potassium-rich minerals like K-feldspar or micas (Manning, 2010).

Trace amounts of titanium dioxide ($TiO_2$) and phosphorus pentoxide ($P_2O_5$) are also present, often less than 1%, and may be associated with accessory minerals such as rutile or apatite (Le Deit et al., 2022). Loss on Ignition (LOI) measures the weight loss from heating, which can be caused by burning organic matter or clays (Hoogsteen et al., 2015; Frangipane et al., 2009; Plater et al., 2015; Heiri et al., 2001). The LOI values in Table 1 are typically low (less than 4%), indicating little organic content or clays in these sandstones. This suggests minimal organic content or clays in these sandstones. Figure 4 illustrates the relative enrichment and depletion of these oxides. Figure 5 compares the chemical composition of Awi sandstones with two reference materials: PAAS (Post Archean Australian Shale) and UCC (Upper Continental Crust). The mineral compositions of Awi sandstones are distinct from those of PAAS and UCC, with notably higher $SiO_2$ levels. Awi sandstone have lower $Al_2O_3$

**Table 1: Major oxides (Wt.%) for sandstones of Awi Formation**

| Sample ID | SiO2 | Al2O3 | Fe2O3T | MnO | MgO | CaO | Na2O | K2O | TiO2 | P2O5 | LOI | TOTAL |
|---|---|---|---|---|---|---|---|---|---|---|---|---|
| AWI A | 53.24 | 16.07 | 10.13 | 0.15 | 4.49 | 6.95 | 3.13 | 2.04 | 1.54 | 0.41 | 0.79 | 98.94 |
| AWI B | 80.26 | 12.03 | 1.33 | 0.01 | 0.27 | 1.21 | 4.46 | 0.63 | 0.05 | 0.01 | 0.63 | 100.89 |
| AWI C | 74.86 | 13.70 | 1.19 | 0.03 | 0.14 | 0.87 | 3.13 | 5.69 | 0.09 | 0.01 | 0.51 | 100.22 |
| AWI D | 62.86 | 15.51 | 9.41 | 0.12 | 0.70 | 0.15 | 0.05 | 1.97 | 0.87 | 0.17 | 8.37 | 100.18 |
| AWI E | 55.25 | 17.56 | 2.95 | 0.10 | 1.22 | 1.55 | 1.18 | 4.50 | 0.82 | 0.17 | 3.70 | 89.00 |
| AWI F | 60.78 | 16.46 | 3.25 | 0.09 | 1.09 | 1.35 | 1.08 | 4.14 | 0.79 | 0.15 | 3.08 | 92.26 |
| AWI G | 66.21 | 15.37 | 2.88 | 0.08 | 0.96 | 1.19 | 0.98 | 3.85 | 0.76 | 0.13 | 2.64 | 95.05 |
| AWI H | 71.63 | 14.28 | 2.56 | 0.07 | 0.83 | 1.04 | 0.89 | 3.58 | 0.73 | 0.11 | 2.21 | 97.93 |
| AWI I | 77.07 | 13.19 | 2.25 | 0.06 | 0.79 | 0.95 | 0.82 | 3.34 | 0.70 | 0.10 | 1.79 | 101.06 |
| AWI J | 62.89 | 16.85 | 3.49 | 0.11 | 1.11 | 1.42 | 1.13 | 4.28 | 0.85 | 0.16 | 3.71 | 96.00 |
| AWI K | 68.32 | 15.71 | 3.12 | 0.09 | 0.98 | 1.29 | 1.03 | 4.05 | 0.78 | 0.14 | 3.17 | 98.68 |
| AWI L | 73.74 | 14.62 | 2.76 | 0.08 | 0.85 | 1.15 | 0.96 | 3.78 | 0.75 | 0.13 | 2.68 | 101.50 |
| AWI M | 79.16 | 13.53 | 2.45 | 0.07 | 0.81 | 1.06 | 0.89 | 3.54 | 0.72 | 0.11 | 2.23 | 104.57 |
| AWI N | 64.65 | 16.35 | 3.39 | 0.10 | 1.08 | 1.39 | 1.10 | 4.18 | 0.82 | 0.16 | 3.68 | 96.90 |
| AWI O | 70.17 | 15.21 | 3.02 | 0.09 | 0.95 | 1.22 | 1.00 | 3.95 | 0.77 | 0.14 | 3.14 | 99.66 |
| PAAS | 62.4 | 18.78 | 7.18 | - | - | 1.29 | 1.19 | 3.68 | 0.99 | 0.16 | - | 95.67 |
| UCC | 66 | 15.2 | 4.5 | - | - | 4.2 | 3.9 | 3.4 | 0.5 | 0.16 | - | 97.87 |

**Table 2: Trace element (ppm) of Awi Sandstones, Calabar Flank**

| | As | Ba | Be | Bi | Cd | Co | Cr | Cu | Hf | Hg |
|---|---|---|---|---|---|---|---|---|---|---|
| AWI A | 2 | 809 | 2 | 2 | 0.5 | 28 | 46 | 35 | 6.6 | 1 |
| AWI B | 2 | 165 | 3 | 2 | 0.5 | 1 | 1 | 6 | 0.5 | 1 |
| AWI C | 2 | 542 | 2 | 2 | 0.5 | 1 | 4 | 12 | 3.1 | 1 |
| AWI D | 5 | 231 | 24 | 2 | 0.5 | 16 | 227 | 27 | 6.2 | 1 |
| AWI E | 5 | 150 | 2 | 2 | 0.5 | 10 | 90 | 15 | 5 | 1 |
| AWI F | 4 | 145 | 2 | 2 | 0.5 | 9 | 80 | 12 | 4 | 1 |
| AWI G | 3 | 240 | 2 | 2 | 0.5 | 8 | 70 | 10 | 3 | 1 |
| AWI H | 2 | 135 | 1 | 2 | 0.5 | 7 | 60 | 8 | 2 | 1 |
| AWI I | 1 | 330 | 1 | 2 | 0.5 | 6 | 50 | 6 | 1 | 1 |
| AWI J | 6 | 155 | 2 | 2 | 0.5 | 11 | 100 | 17 | 6 | 1 |
| AWI K | 5 | 150 | 2 | 2 | 0.5 | 10 | 90 | 15 | 5 | 1 |
| AWI L | 4 | 245 | 2 | 2 | 0.5 | 9 | 80 | 12 | 4 | 1 |
| AWI M | 3 | 140 | 2 | 2 | 0.5 | 8 | 70 | 10 | 3 | 1 |
| AWI N | 2 | 135 | 1 | 2 | 0.5 | 7 | 60 | 8 | 2 | 1 |
| AWI O | 1 | 430 | 1 | 2 | 0.1 | 6 | 50 | 6 | 1 | 1 |
| Mean | 3.13 | 266.80 | 3.27 | 2.00 | 0.47 | 9.13 | 71.87 | 13.27 | 3.49 | 1.00 |

**Table 2: Trace element (ppm) of Awi Sandstones, Calabar Flank (Contd.)**

| | Mo | Ni | Pb | Rb | Sc | Sr | Ta | Th | Nb | U | Y | Zn | Zr |
|---|---|---|---|---|---|---|---|---|---|---|---|---|---|
| AWI A | 2 | 28 | 7 | 40 | 25.1 | 404 | 1 | 2.9 | 11.2 | 0.5 | 43 | 116 | 272 |
| AWI B | 2 | 5 | 16 | 20 | 1.1 | 290 | 1 | 0.5 | 6.8 | 0.5 | 4 | 18 | 18 |
| AWI C | 2 | 3 | 39 | 150 | 2.4 | 148 | 1 | 13.4 | 9.02 | 6.8 | 17 | 15 | 78 |
| AWI D | 3 | 29 | 23 | 180 | 14.3 | 89 | 6 | 13.9 | 6.4 | 5.2 | 20 | 59 | 245 |
| AWI E | 1 | 50 | 30 | 150 | 2.3 | 100 | 1 | 10 | 10.73 | 3 | 15 | 60 | 100 |
| AWI F | 2 | 45 | 25 | 140 | 12.1 | 90 | 1 | 8 | 12.26 | 2 | 13 | 55 | 90 |
| AWI G | 2 | 40 | 20 | 130 | 3.1 | 80 | 1 | 6 | 27.4 | 1.5 | 11 | 50 | 80 |
| AWI H | 2 | 35 | 15 | 120 | 11.1 | 70 | 1 | 4 | 17.9 | 1 | 9 | 45 | 70 |
| AWI I | 3 | 30 | 10 | 110 | 2.2 | 60 | 0.5 | 2 | 10.2 | 0.5 | 7 | 40 | 60 |
| AWI J | 1.2 | 55 | 35 | 160 | 4.2 | 110 | 1.5 | 12 | 9.73 | 4 | 16 | 65 | 110 |
| AWI K | 1 | 50 | 30 | 150 | 3.6 | 100 | 1 | 10 | 10.6 | 3 | 15 | 60 | 100 |
| AWI L | 2 | 45 | 25 | 140 | 7.5 | 90 | 1 | 8 | 7.8 | 2 | 13 | 55 | 90 |
| AWI M | 3 | 40 | 20 | 130 | 8.2 | 80 | 1 | 6 | 8.4 | 1.5 | 11 | 50 | 80 |
| AWI N | 1 | 35 | 15 | 120 | 6.1 | 70 | 1 | 4 | 12.6 | 1 | 9 | 45 | 70 |
| AWI O | 2 | 30 | 10 | 110 | 2.6 | 60 | 0.5 | 2 | 15.8 | 0.5 | 7 | 40 | 60 |
| Mean | 1.95 | 34.67 | 21.33 | 123.33 | 7.06 | 122.73 | 1.30 | 6.85 | 11.79 | 2.20 | 14.00 | 51.53 | 101.53 |

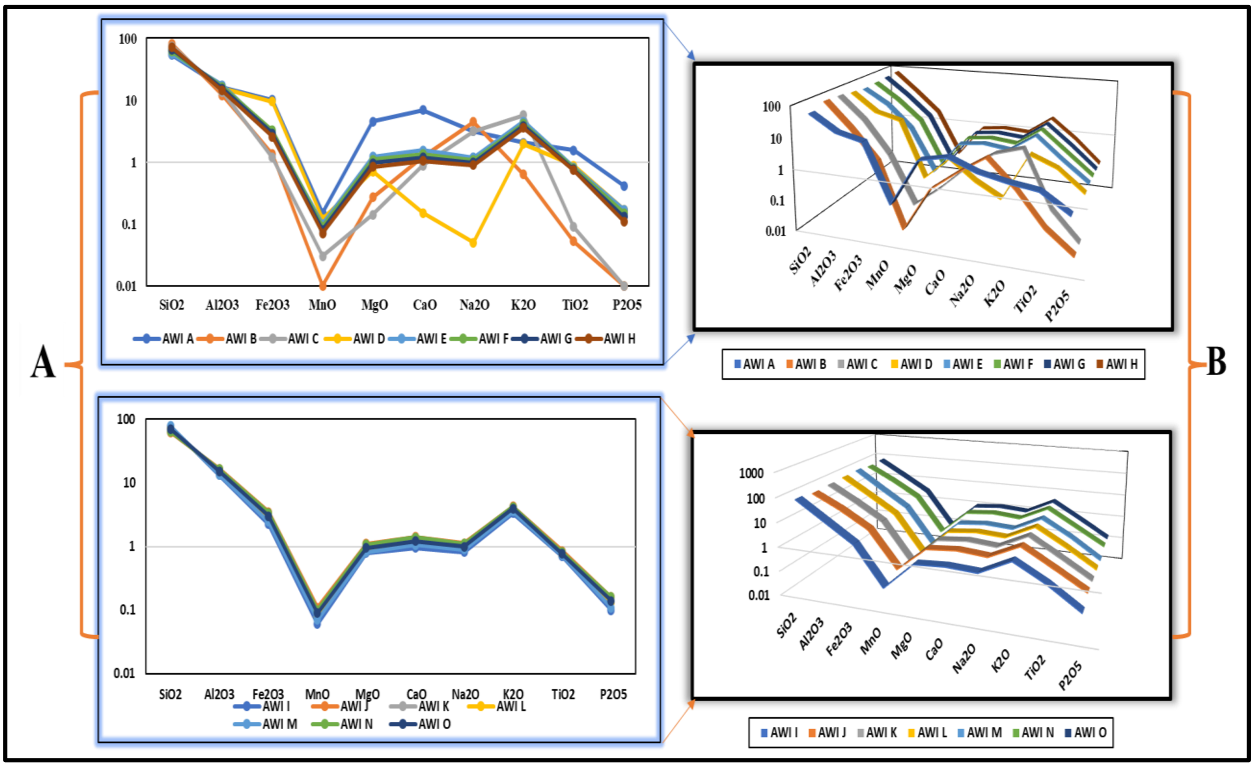


FIG. 4A - 2D Spatial Distribution Patterns of Major Oxides (wt. %) of Awi Formation,
B - 3D Spatial Distribution Patterns of Major Oxides (wt. %) of Awi Formation

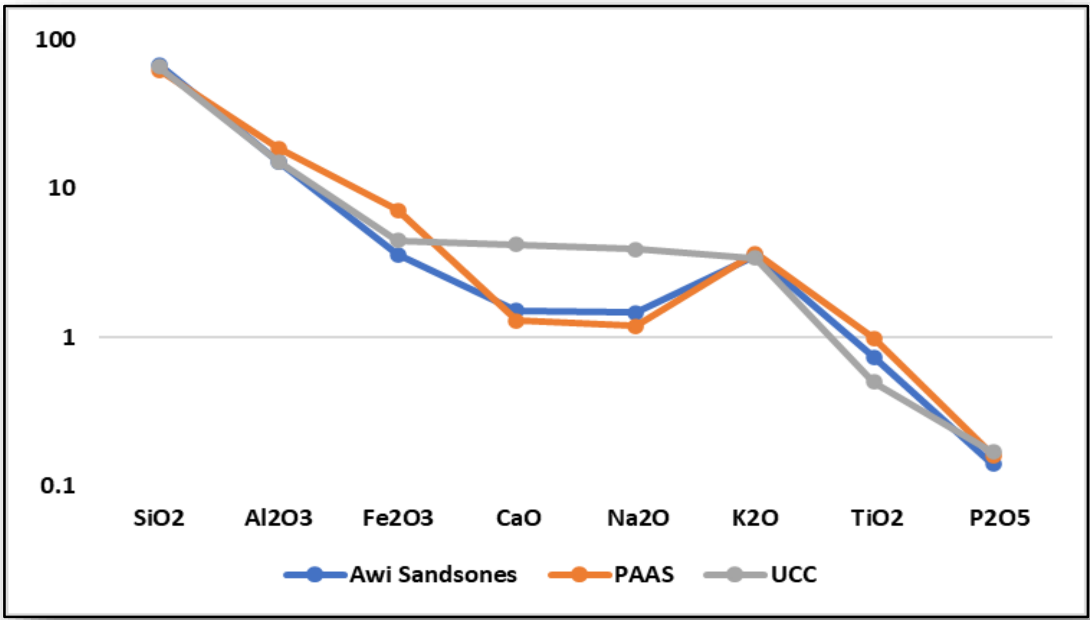


FIG.5. Spatial distribution patterns of Major Oxides (wt. %) from Awi Sandstones to PAAS and UCC (Taylor and McLennan, 1983)

levels compared to PAAS but similar to UCC, indicating the presence of aluminum-bearing minerals such as feldspar, albeit in smaller quantities than PAAS. Furthermore, the $Fe_2O_3$ levels in Awi sandstones are lower than both PAAS and UCC. The CaO content in Awi sandstones is marginally higher than in PAAS but lower than in
UCC. Awi sandstones also contain slightly higher $Na_2O$ levels than PAAS, but lower than in UCC. Additionally, the $K_2O$ levels in Awi sandstones are slightly lower than in PAAS but higher than in UCC. Awi sandstones exhibit lower levels of $TiO_2$ compared to PAAS but slightly higher levels compared to UCC. In general, the geochemistry of Awi sandstone bears a closer resemblance to UCC than to PAAS.

The Pearson correlation matrix for the major oxides, as displayed in Table 3, is statistically significant at the 0.05 level (two-tailed). This matrix aids in understanding the evolutionary path of the melt. Table 3 reveals a robust negative correlation between $SiO_2$ and $Al_2O_3$, $Fe_2O_3$, MnO, $TiO_2$, $P_2O_5$, and MgO, and a weaker negative correlation between $SiO_2$ and $K_2O$. The correlation between $SiO_2$ and $Al_2O_3$ suggests feldspar crystallization. In order to pinpoint the specific feldspar end-member undergoing crystallization, the correlations between $SiO_2$ and $K_2O$, and $SiO_2$ and $Na_2O$ are compared. The negative correlation between $SiO_2$ and $K_2O$ indicates the crystallization of K-feldspar, such as orthoclase. The presence of a negative correlation between $SiO_2$ and $Fe_2O_3$ points to the formation of olivine (fayalite-$Fe_2SiO_4$) or pyroxene (ferrosilite-$Fe_2Si_2O_6$) through crystallization. The relationship between $SiO_2$ and MgO indicates the potential crystallization of pyroxene (enstatite-$Mg_2Si_2O_6$) or olivine (forsterite-$Mg_2SiO_4$). An inverse correlation between $SiO_2$ and $TiO_2$ suggests the potential formation of titanium-bearing minerals such as ilmenite ($FeTiO_3$) or rutile ($TiO_2$). The negative correlation between $SiO_2$ and $P_2O_5$ indicates the potential formation of phosphate minerals like apatite. Figures 6 and 7 present Harker's plot and the density ellipse plot, respectively, which offer a visual representation of Pearson's correlation matrix.

**Table 3. Pearson's correlation matrix for the major oxides (wt.%) of Awi sandstone**

| | SiO2 | Al2O3 | Fe2O3T | MnO | MgO | CaO | Na2O | K2O | TiO2 | P2O5 |
|---|---|---|---|---|---|---|---|---|---|---|
| SiO2 | 1 | | | | | | | | | |
| Al2O3 | -0.9006 | 1 | | | | | | | | |
| Fe2O3T | -0.6422 | 0.39123 | 1 | | | | | | | |
| MnO | -0.8346 | 0.79478 | 0.79311 | 1 | | | | | | |
| MgO | -0.6549 | 0.40608 | 0.71013 | 0.71904 | 1 | | | | | |
| CaO | -0.5282 | 0.24982 | 0.58238 | 0.5282 | 0.96443 | 1 | | | | |
| Na2O | 0.16845 | -0.4173 | -0.1029 | -0.4384 | 0.18248 | 0.42319 | 1 | | | |
| K2O | -0.0929 | 0.37724 | -0.4364 | 3.3E-17 | -0.2484 | -0.2699 | -0.3523 | 1 | | |
| TiO2 | -0.7222 | 0.63471 | 0.7397 | 0.93748 | 0.83132 | 0.65957 | -0.3851 | -0.0887 | 1 | |
| P2O5 | -0.7794 | 0.60167 | 0.81373 | 0.90314 | 0.94413 | 0.82864 | -0.1058 | -0.1896 | 0.95125 | 1 |

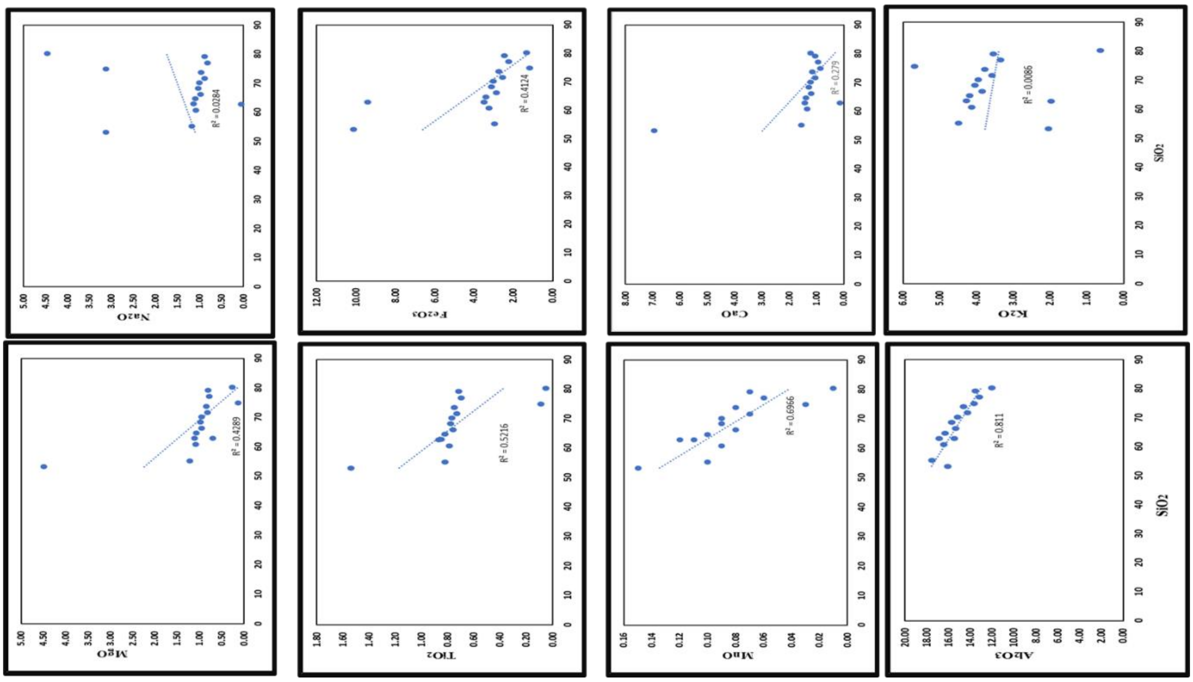

**FIG. 6. Harker's variation diagram of silica ($SiO_2$) versus major oxides**

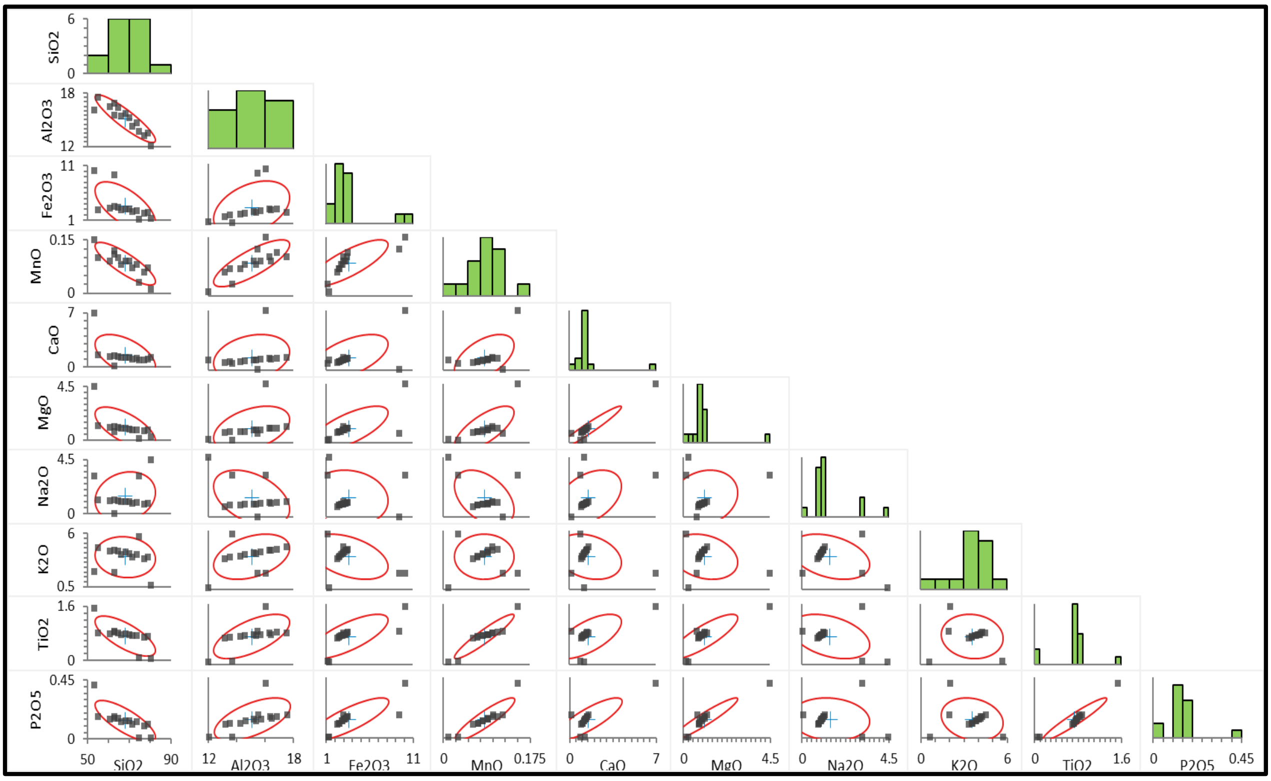


FIG.7 Scatter Plot of Correlation Matrix with Density ellipse and Histogram of Major Oxides (wt. %) of Awi Sandstone

**Metal Enrichment**

**Trace element geochemistry**

In Table 4, you can find the data regarding trace metal enrichment and depletion. According to Adamu et al. (2020), the classification of metal enrichment and depletion is based on average concentrations and consists of three groups: highly enriched (> 50 ppm), moderately enriched (1-50 ppm), and deficient (< 1 ppm). The metals classified as highly enriched are barium (Ba) at 266.80 ppm, chromium (Cr) at 71.87 ppm, rubidium (Rb) at 123.33 ppm, strontium (Sr) at 122.73 ppm, zinc (Zn) at 51.53 ppm, and zircon (Zr) at 101.53 ppm. Other metals such as arsenic (As) are at 3.13 ppm, beryllium (Be) at 3.27 ppm, bismuth (Bi) at 2 ppm, cobalt (Co) at 9.13 ppm, copper (Cu) at 13.27 ppm, hafnium (Hf) at 3.49 ppm, mercury (Hg) at 1 ppm, molybdenum (Mo) at 1.95 ppm, and nickel (Ni) at 34.67 ppm, lead (Pb) at 21.33 ppm, and scandium (Sc) at 7.06 ppm. The samples show significant depletion of only one element, cadmium (Cd), with a concentration of 0.47 ppm. The enrichment and depletion of various trace elements are visually represented in Figure 8. Figures 9a-9f illustrate the spatial distribution map of highly enriched metals within the research area. The maps were generated using Arcmap 10.8. The spatial plots indicate a concentration of barium in the NE-SW trend, while zircon and rubidium are more prevalent in the western region. Higher quantities of zinc, strontium, and chromium are found in the Northwest region. The enrichment of elements like Ba, Rb, Sr, Cr, Zn, Ni, Y, and Cu can possibly reflect the presence of felsic or intermediate igneous rocks. These elements are often associated with hydrothermal mineralization processes. The presence of elevated levels of transition metals (like Cr, Ni, and Cu) could indicate contributions from mafic or ultramafic rocks, potentially linked to mantle-derived materials or deep crustal sources. A comparison of metal enrichment in Awi sandstones with that of Nkporo and Ekenkpon shales, as described in Adamu et al. (2020) and presented in Table 4, indicates strong enrichment of Ba, Rb, Zn, Zr, Sr, and Cr in both formations. The concentration of Ba in Nkporo shale (342 ppm) and Ekenkpon shale (281.87 ppm) is higher on average than that of Awi sandstones (266.80 ppm), and the concentration of shale (281.87 ppm) surpasses that of Awi sandstones (266.80 ppm). Awi sandstones have a higher average Cr concentration (71.87 ppm) than Nkporo shale (64 ppm) but slightly lower than Ekenkpon shale (74.27 ppm). The mean Rb concentration (123.33 ppm) observed in Awi sandstones exceeds that in Nkporo shale (90.9 ppm) and Ekenkpon shale (93.33 ppm). The average concentrations of Sr in Nkporo shale (417 ppm) and Ekenkpon shale.

**Table 4: Comparison of average concentrations of trace elements of Awi sandstones to average concentrations of Nkporo and Ekenkpon shale.**

| | 1 | 2 | |
|---|---|---|---|
| **Trace Element(ppm)** | **Awi Sandstones** | **Nkporo shale** | **Ekenkpon shale** |
| **As** | **3.13** | **4.38** | **3.42** |
| **Ba** | **266.80** | **342** | **281.17** |
| **Be** | **3.27** | **1.93** | **1.48** |
| **Bi** | **2.00** | **0.18** | **0.18** |
| **Cd** | **0.47** | **0.16** | **0.06** |
| **Co** | **9.13** | **20.42** | **18.58** |
| **Cr** | **71.87** | **64** | **74.27** |
| **Cu** | **13.27** | **22.62** | **25.97** |
| **Hf** | **3.49** | **2.48** | **2.58** |
| **Hg** | **1.00** | **0.01** | **0.01** |
| **Mo** | **1.95** | **35.76** | **31.87** |
| **Ni** | **34.67** | **55.68** | **59.97** |
| **Pb** | **21.33** | **25.94** | **21.85** |
| **Rb** | **123.33** | **90.9** | **93.33** |
| **Sc** | **7.06** | **10.81** | **12.21** |
| **Sr** | **122.73** | **417** | **250.87** |
| **Ta** | **1.30** | **0.77** | **1.33** |
| **Th** | **6.85** | **15.86** | **17.2** |
| **Nb** | **11.79** | **13** | **12.58** |
| **U** | **2.20** | **5.8** | **5.5** |
| **Y** | **14.00** | **45.22** | **29.67** |
| **Zn** | **51.53** | **115.7** | **67.5** |
| **Zr** | **101.53** | **86.28** | **96.93** |

1 – This study
2 – Adamu et al., 2020

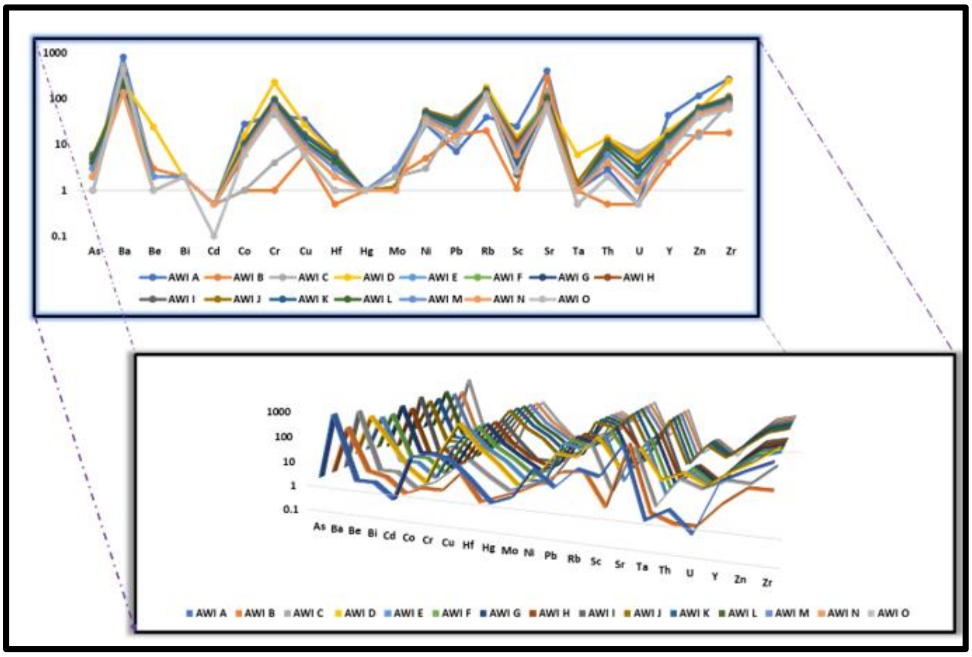


FIG.8: 2D and 3D Spatial Distribution Patterns of Trace Elements (ppm) of Awi Formation

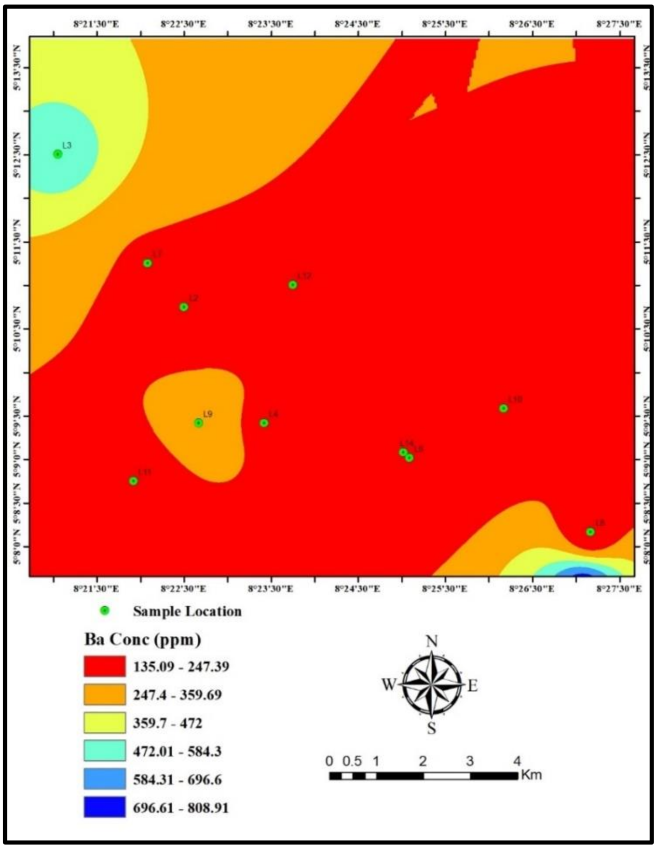


FIG. 9a. Geochemical map of Ba concentration (ppm) in the study area

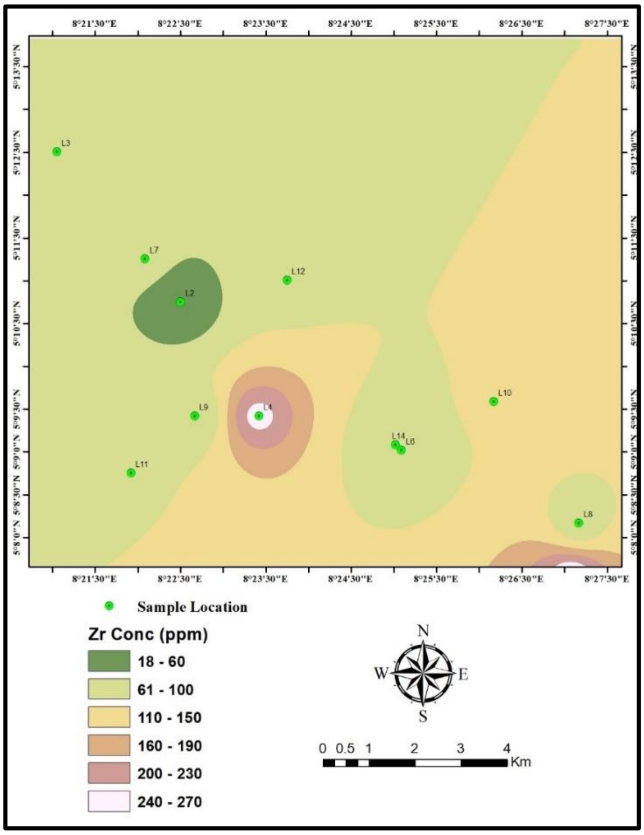


FIG. 9b. Geochemical map of Zr concentration (ppm) in the study area

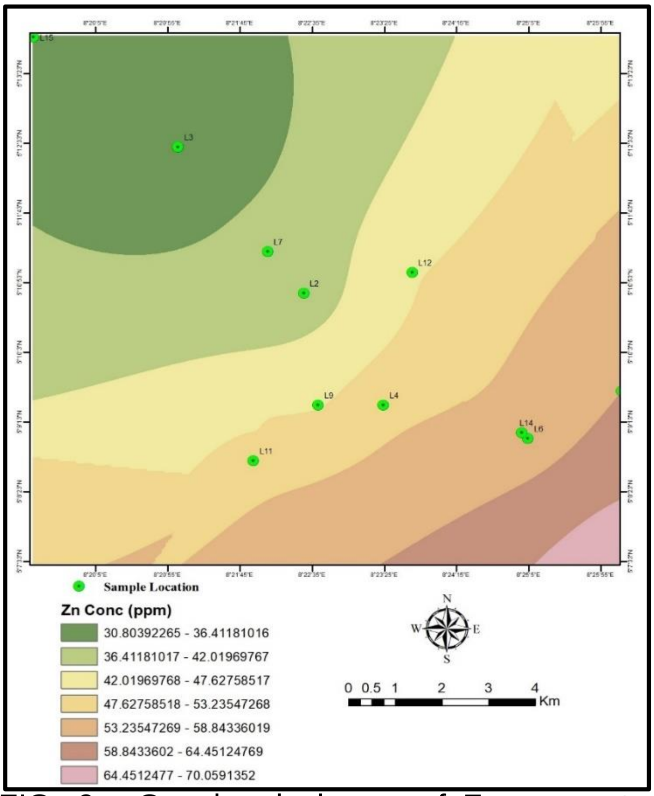


FIG. 9c. Geochemical map of Zn concentration (ppm) in the study area

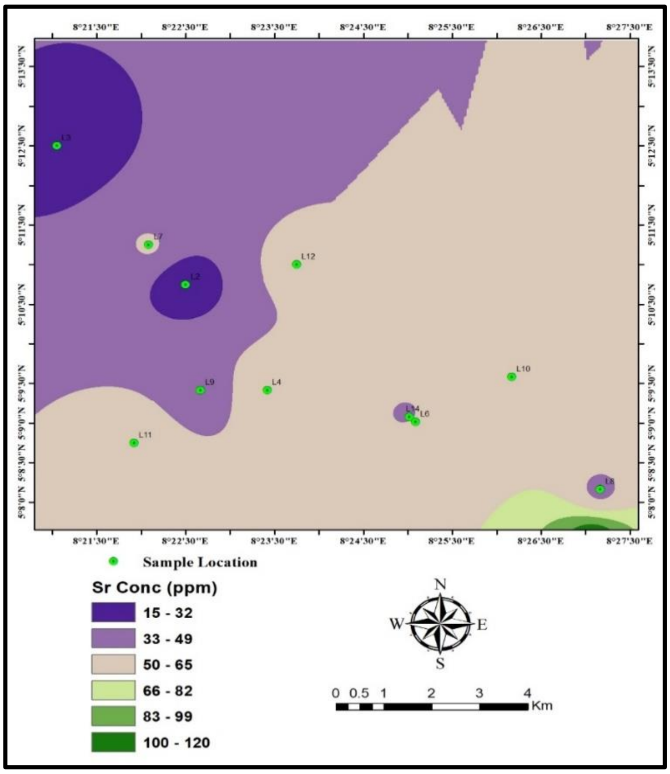


FIG.9d Geochemical map of Sr concentration (ppm) in the study area

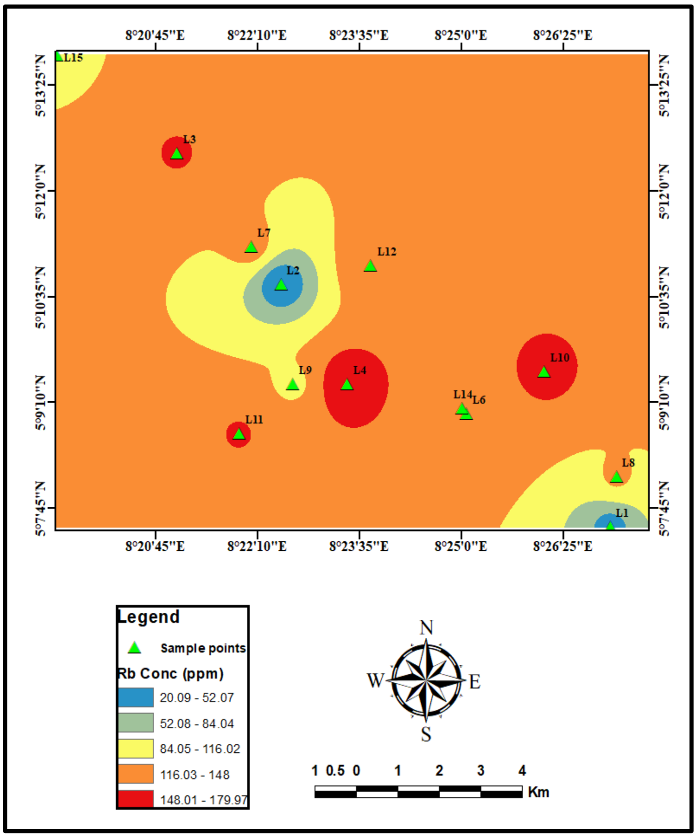


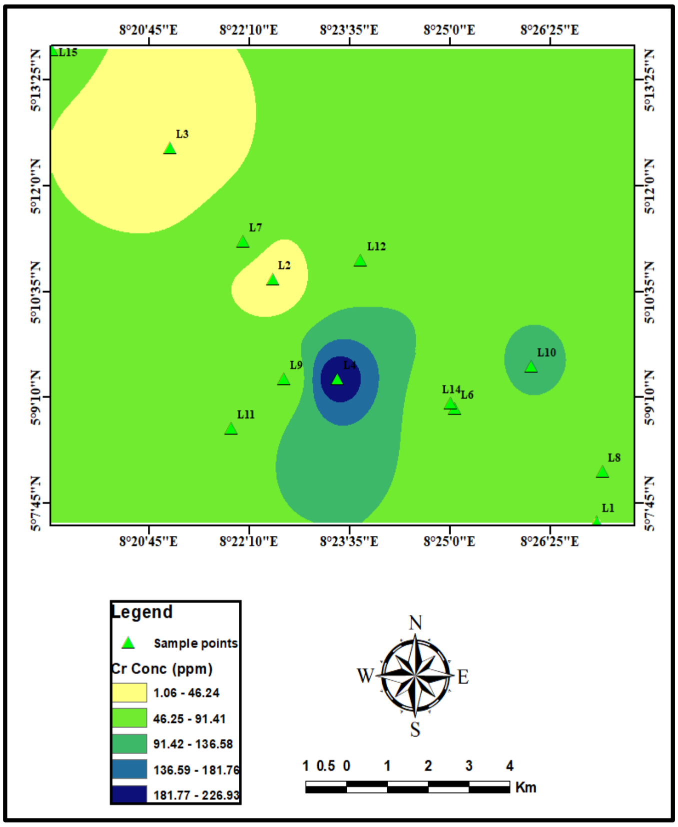


FIG. 9f. Geochemical map of Cr concentration (ppm) in the study area

shale (250.87 ppm) are both higher than that in Awi sandstones (122.73 ppm). The Zn concentrations in Nkporo shale (115.7 ppm) and Ekenkpon shale (67.5 ppm) were higher compared to the Awi Formation (51.53 ppm). Awi sandstones had a higher average Zr concentration (101.53 ppm) than Nkporo shale (86.28 k ppm) and Ekenkpon shale (96.93 ppm). The presence of highly enriched metals in Awi sandstones, in association with Nkporo and Ekenkpon shales, indicates the significant role played by these shales in the mineralization process.

*3.2.2 Rare Earth Element (REE) geochemistry*

The concentrations of light rare earth elements (LREE), middle rare earth elements (MREE), and heavy rare earth elements (HREE) in the Awi sandstones are presented in Table 5 (Weng et al., 2015). LREEs, such as lanthanum (La), cerium (Ce), and neodymium (Nd), are included. MREEs consist of samarium (Sm) and europium (Eu), while the HREEs are terbium (Tb), lutetium (Lu), and yttrium (Y). An analysis of the data reveals that LREEs, with an average concentration of 95.16 ppm, are more enriched compared to the average concentrations of 5.77 ppm for MREEs and 24.03 ppm for HREEs. The samples analyzed had concentrations normalized to five reference standards: Chondrite (McLennan, 2003), Post Archean Australian Shales (PAAS) (McLennan, 1981), Upper Continental Crust (UCC) (Taylor and McLennan, 1983), North America Shale Composite (NASC) (Gromet et al., 1984), and European Shale (ES) (Prego et al., 2009). Normalized concentrations can be found in Table 6. After normalization, concentrations were presented to illustrate enrichment and depletion (Figure 10). Concentrations lower than one ppm are considered depleted, while those above one ppm are considered enriched. When compared to chondrite, the normalized amounts of REEs in Awi sandstones show that LREEs are more abundant than MREEs and HREEs. In contrast, some other reference standards indicate a reduction in these components. The average rare earth element (REE) levels in Awi sandstone were contrasted with those of Nkporo and Ekenkpon shales (see Table 7). The increase in LREE relative to HREE observed could indicate a preferential removal or retention of HREE in heavy minerals like zircon, monazite, or xenotime during sedimentary or metamorphic processes

**Table 5: The elemental concentrations (ppm) of LREE, MREE, and HREE in the Awi sandstones**

| REE | La | Ce | Nd | Sm | Eu | Tb | Yb | Lu | Y | LREE | MREE | HREE | TREE |
|---|---|---|---|---|---|---|---|---|---|---|---|---|---|
| AWI A | 23.6 | 57 | 37 | 8.2 | 1.5 | 1 | 3.5 | 0.27 | 43 | 117.6 | 9.7 | 47.77 | 175.07 |
| AWI B | 0.8 | 3 | 5 | 0.5 | 0.1 | 0.5 | 0.3 | 0.05 | 4 | 8.8 | 0.6 | 4.85 | 14.25 |
| AWI C | 15.6 | 30 | 11 | 3.3 | 0.5 | 0.5 | 1.5 | 0.18 | 17 | 56.6 | 3.8 | 19.18 | 79.58 |
| AWI D | 38.9 | 80 | 30 | 6.6 | 1.1 | 0.5 | 1.5 | 0.11 | 20 | 148.9 | 7.7 | 22.11 | 178.71 |
| AWI E | 0.7 | 2.4 | 4.5 | 0.52 | 0.2 | 0.56 | 0.25 | 0.3 | 5 | 7.6 | 0.72 | 6.11 | 14.43 |
| AWI F | 20.7 | 35.5 | 24.45 | 4.95 | 1.41 | 0.71 | 2.94 | 0.23 | 17.5 | 80.65 | 6.36 | 21.38 | 108.39 |
| AWI G | 25.8 | 69.8 | 36.8 | 4.42 | 2.1 | 0.57 | 1.38 | 0.35 | 22.21 | 132.4 | 6.52 | 24.51 | 163.43 |
| AWI H | 0.6 | 3 | 6 | 0.55 | 0.33 | 0.51 | 0.29 | 0.05 | 5 | 9.6 | 0.88 | 5.85 | 16.33 |
| AWI I | 39.4 | 70.7 | 40.9 | 6.21 | 1.12 | 0.87 | 0.45 | 0.16 | 22.6 | 151 | 7.33 | 24.08 | 182.41 |
| AWI J | 35.16 | 41.16 | 31.7 | 7.62 | 1.42 | 0.52 | 1.45 | 0.44 | 25.51 | 108.02 | 9.04 | 27.92 | 144.98 |
| AWI K | 50.5 | 90.56 | 45.65 | 8.1 | 1.9 | 0.92 | 2.61 | 0.72 | 40.2 | 186.71 | 10 | 44.45 | 241.16 |
| AWI L | 24.9 | 67.2 | 39.1 | 3.2 | 1.08 | 0.77 | 3.95 | 0.44 | 23.8 | 131.2 | 4.28 | 28.96 | 164.44 |
| AWI M | 20.5 | 43.3 | 28.89 | 5.7 | 0.52 | 0.53 | 1.56 | 0.25 | 26.5 | 92.69 | 6.22 | 28.84 | 127.75 |
| AWI N | 21.7 | 42.5 | 15.3 | 4.97 | 0.92 | 0.65 | 1.97 | 0.27 | 18.6 | 79.5 | 5.89 | 21.49 | 106.88 |
| AWI O | 16.5 | 75.8 | 23.9 | 6.52 | 1.04 | 0.87 | 1.6 | 0.43 | 30.1 | 116.2 | 7.56 | 33 | 156.76 |
| MEAN | 22.36 | 47.46 | 25.35 | 4.76 | 1.02 | 0.67 | 1.68 | 0.28 | 21.40 | 95.16 | 5.77 | 24.03 | 124.97 |

**Table 6. Awi Sandstones, reference values (Chondrite, PAAS, NASC, U`CC, and ES) of REEs and normalization ratios of Awi Sandstones to reference values of REEs**

| REEs | La | Ce | Nd | Sm | Eu | Tb | Yb | Lu | Y |
|---|---|---|---|---|---|---|---|---|---|
| Awi Sandstones | 22.357 | 47.461 | 25.346 | 4.757 | 1.016 | 0.665 | 1.683 | 0.283 | 21.401 |
| PAAS | 38.2 | 79.6 | 33.9 | 5.55 | 1.08 | 0.774 | 2.82 | 0.433 | 27 |
| UCC | 30 | 64 | 26 | 4.5 | 0.88 | 0.64 | 2.2 | 0.3 | 22 |
| NASC | 32 | 70 | 31 | 5.55 | 1.24 | 0.85 | 3.1 | 0.48 | 27 |
| ES | 41.1 | 81.3 | 40.1 | 7.3 | 1.52 | 1.05 | 3.29 | 0.58 | 31.8 |
| Chondrite | 0.367 | 0.957 | 0.711 | 0.231 | 0.087 | 0.058 | 0.248 | 0.0381 | 2.1 |
| Awi Sandstones/PAAS | 0.585 | 0.596 | 0.748 | 0.857 | 0.941 | 0.860 | 0.597 | 0.654 | 0.793 |
| Awi Sandstones/UCC | 0.745 | 0.742 | 0.975 | 1.057 | 1.155 | 1.040 | 0.765 | 0.944 | 0.973 |
| Awi Sandstones/NASC | 0.699 | 0.678 | 0.818 | 0.857 | 0.819 | 0.783 | 0.543 | 0.590 | 0.793 |
| Awi Sandstones/ES | 0.544 | 0.584 | 0.632 | 0.652 | 0.668 | 0.634 | 0.512 | 0.489 | 0.673 |
| Awi Sandstones/Chondrite | 60.919 | 49.594 | 35.648 | 20.595 | 11.678 | 11.471 | 6.788 | 7.437 | 10.191 |

**Table 7. Comparison of average concentrations of REEs of Awi sandstones to average concentrations of Nkporo and Ekenkpon Shale**

| Sample | La | Ce | Nd | Sm | Eu | Tb | Yb | Lu |
|---|---|---|---|---|---|---|---|---|
| Awi Sandstones | 22.36 | 47.46 | 25.35 | 4.76 | 1.02 | 0.67 | 1.68 | 0.28 |
| Nkporo Shale | 84.44 | 157.50 | 45.46 | 10.50 | 2.86 | 1.83 | 4.12 | 0.66 |
| Ekenkpon shale | 51.67 | 104.45 | 36.05 | 7.72 | 0.64 | 0.86 | 2.08 | 0.26 |

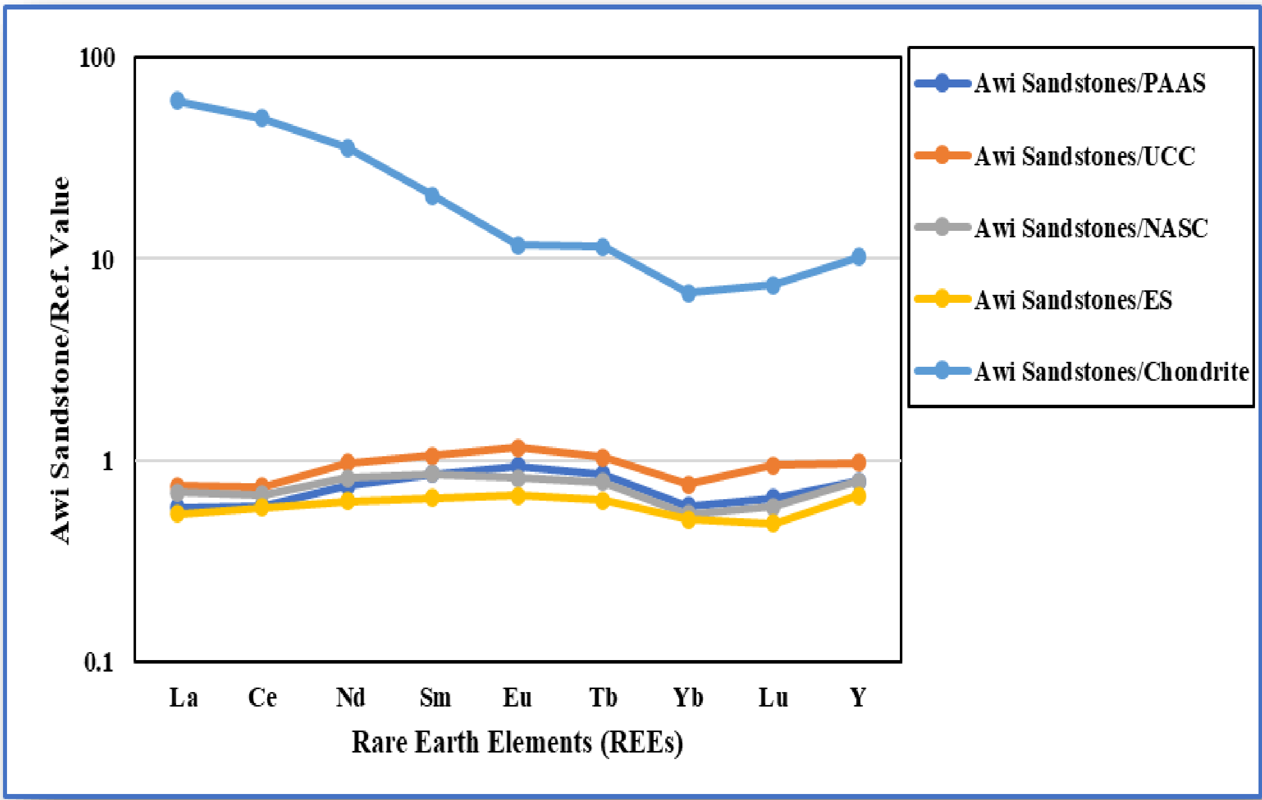


FIG. 10. Normalized patterns of REEs of Awi Sandstones to reference values (chondrite, PAAS, UCC, NASC, ES)

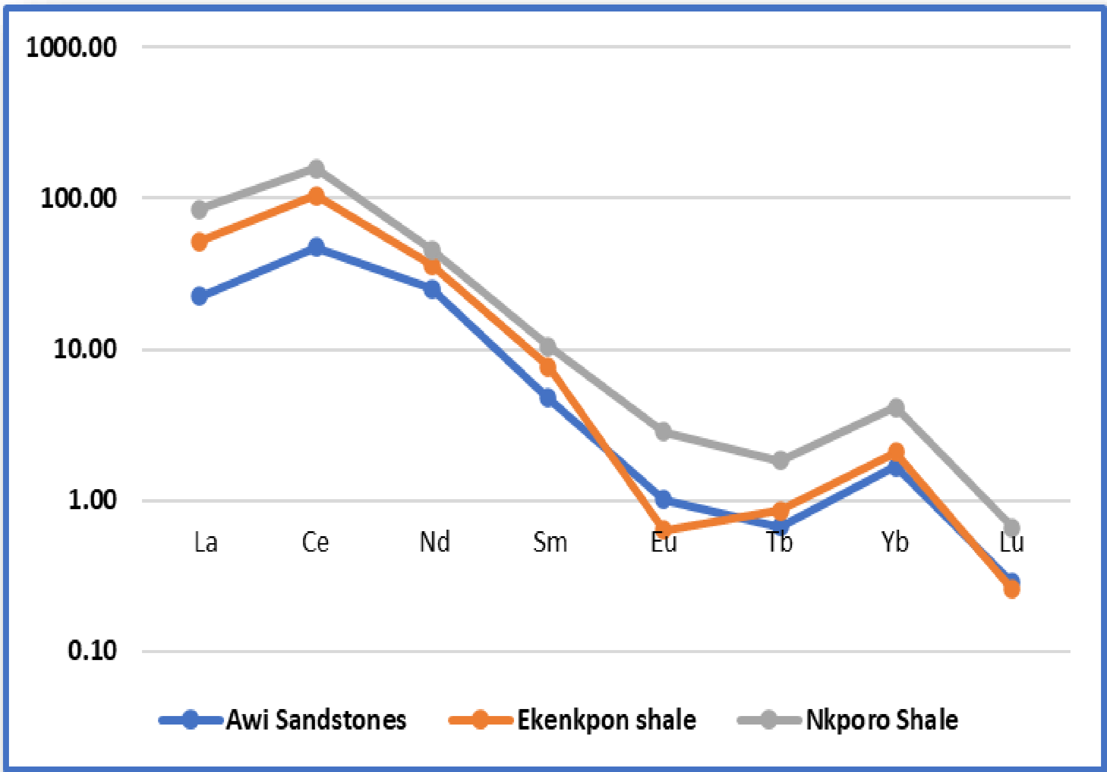


FIG. 11. Spatial distribution patterns of REEs (ppm) from Awi Sandstones compared to Nkporo and Ekenkpon Shale (Adamu *et al.,* 2020)

Figure 11 illustrates that Nkporo shale contains a higher amount of light rare earth elements (LREEs) compared to Ekenkpon shale and Awi sandstone.

**Provenance**

Analysis of the $TiO_2$ vs Zr plot (Hayashi et al., 1997) reveals that the majority of sample points fall within the intermediate to felsic range (Figure 12), suggesting that the Awi sandstones originate from rocks within this compositional range. This observation is further supported by the Discriminant Function diagram for provenance (Figure 13), which indicates contributions from the region's mafic rocks (amphibolite) in certain points. Intermediate and felsic rocks are commonly associated with continental crust environments such as volcanic arcs, continental margins, and orogenic belts (Sun et al., 2013), while mafic rocks are typically found along divergent plate boundaries, such as mid-ocean ridges. The plot of Th/Yb against Zr/Y, which separates tholeiitic, transitional, and calc-alkaline fields, indicates that the protolith of Awi sandstone is calc-alkaline (refer to Figure 14). According to Miyashiro's (1974) FeOt/MgO against $SiO_2$ discrimination plots (see Figure 15) and the AFM plot distinguishing between the calc-alkaline and tholeiite series (based on Irvine and Baragar, 1971) (check Figure 16), it also confirms this calc-alkaline nature. The alkaline series can be classified as either high-K calc-alkaline or just calc-alkaline. As shown in Figure 17, Awi sandstones are primarily high-K calc-alkaline, which is supported by the Co-Th discrimination plot by Hastie et al. (2007) (see Figure 18). The discrimination plot in Figure 19, based on $(Al_2O_3+CaO)/(FeOt+Na_2O+K_2O)$ vs $100(MgO+FeOt+TiO_2)/SiO_2$ ratio as per Sylvester (1989), indicates that Awi sandstones' protolith is notably peraluminous. Per Okunola et al. (2013), peraluminous rocks are characterized by an Aluminum Saturation

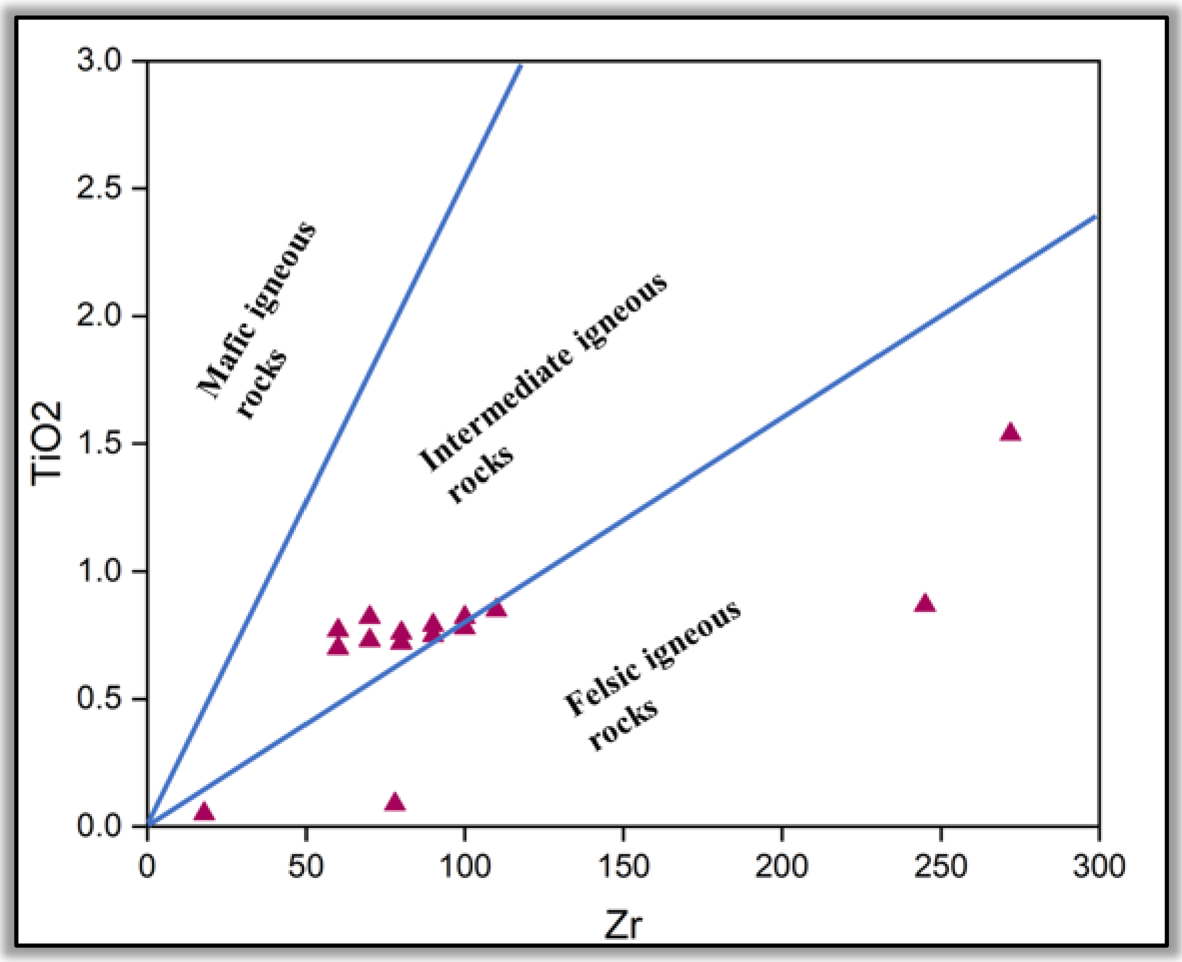


FIG. 12. Discrimination plot of $TiO_2$–Zr showing mafic, intermediate and felsic igneous rocks (fields after Hayashi *et al.,* 1997)

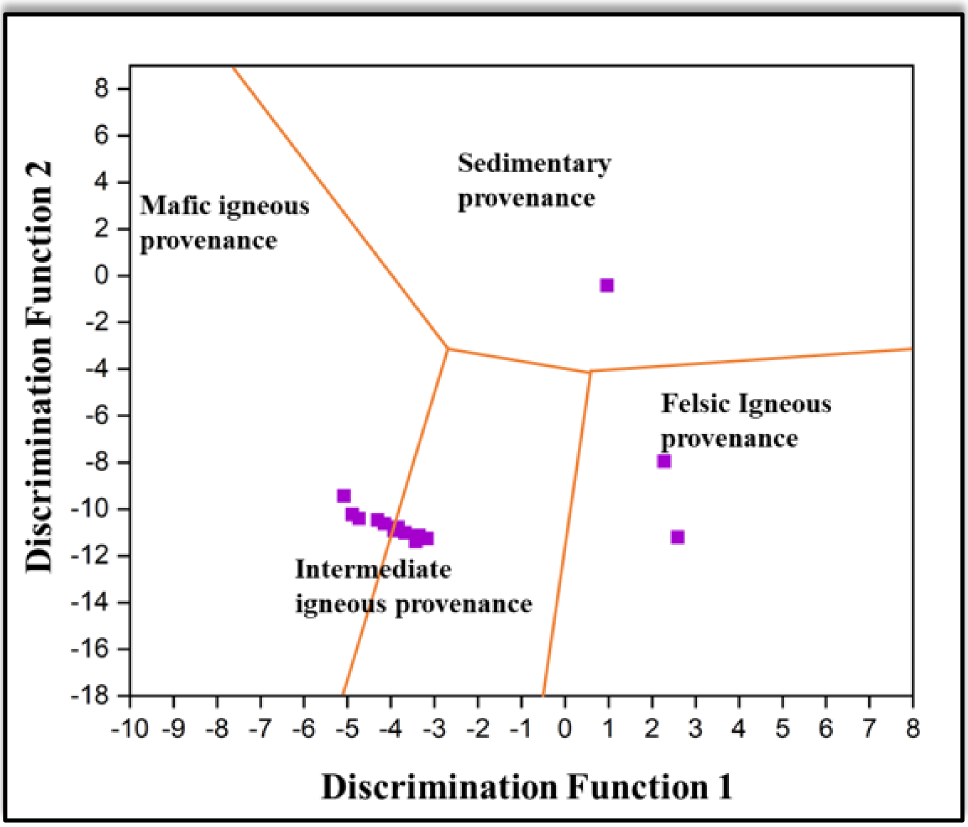


FIG. 13. Major element Discriminant Function diagram for provenance (fields after Murali *et al.* 1983)

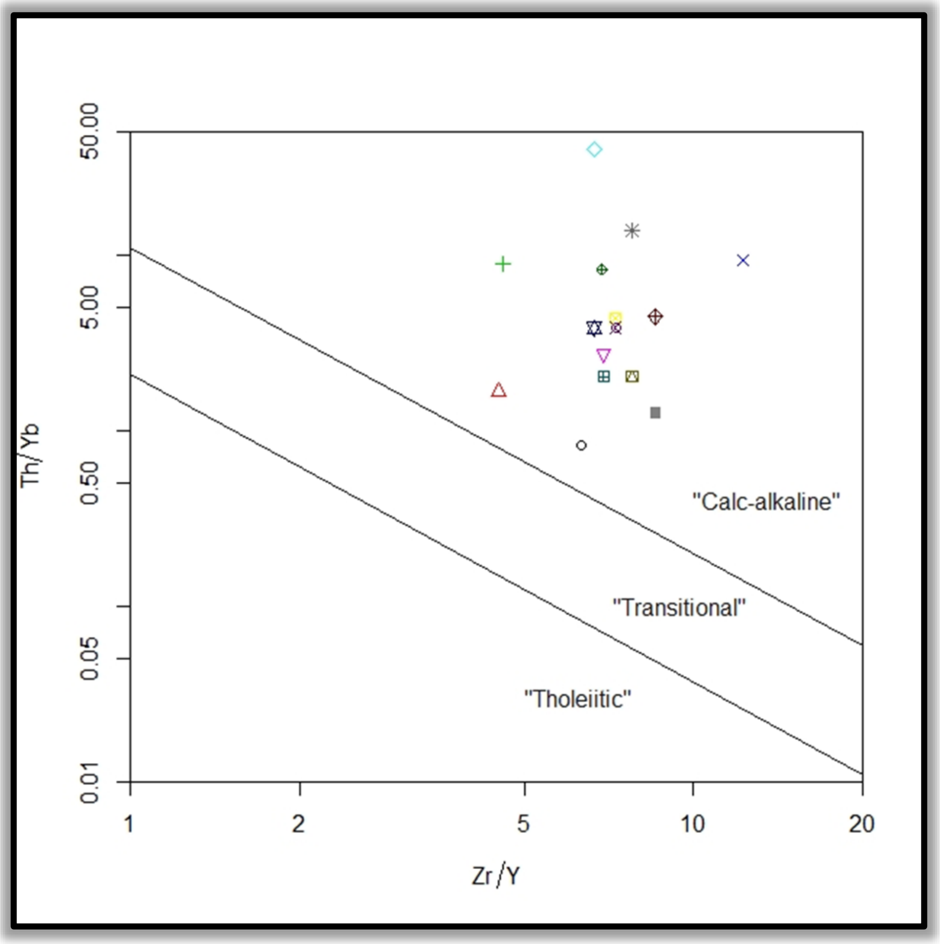


FIG. 14. Discrimination plots of Th/Yb versus Zr/Y (fields after Ross and Bedard 2009)

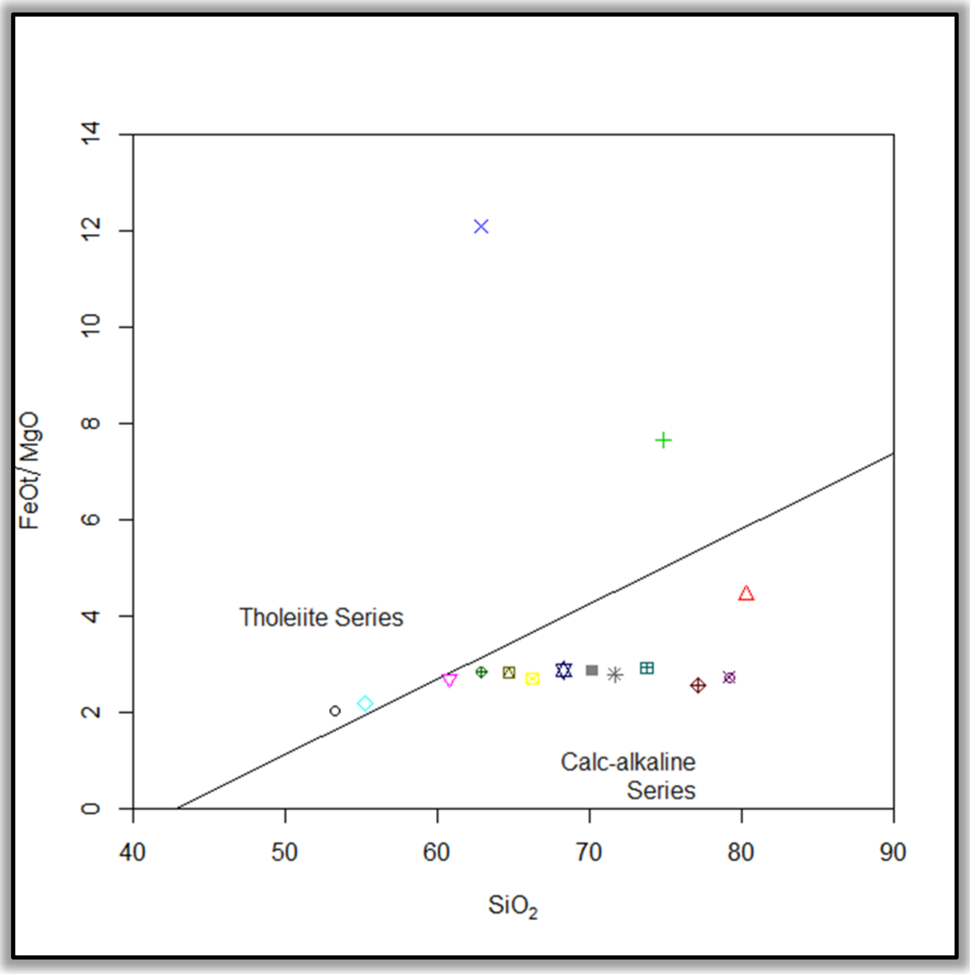


FIG. 15. Discrimination plots of FeOt/MgO versus $SiO_2$ (After Miyashiro 1974)

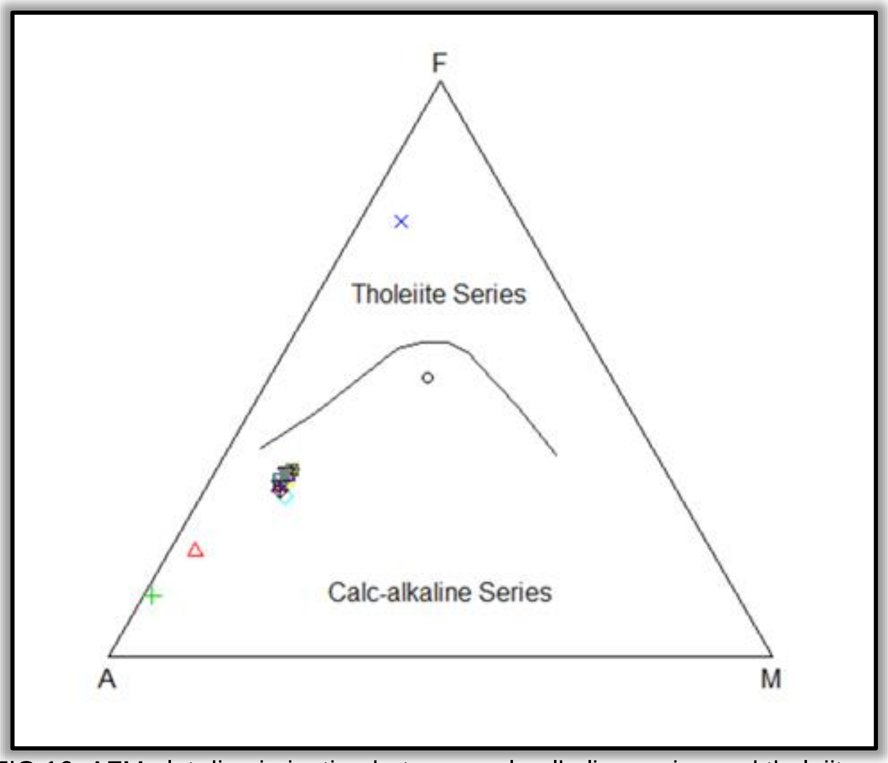


FIG.16. AFM plot discriminating between calc-alkaline series and tholeiite series (After Irvine and Baragar, 1971)

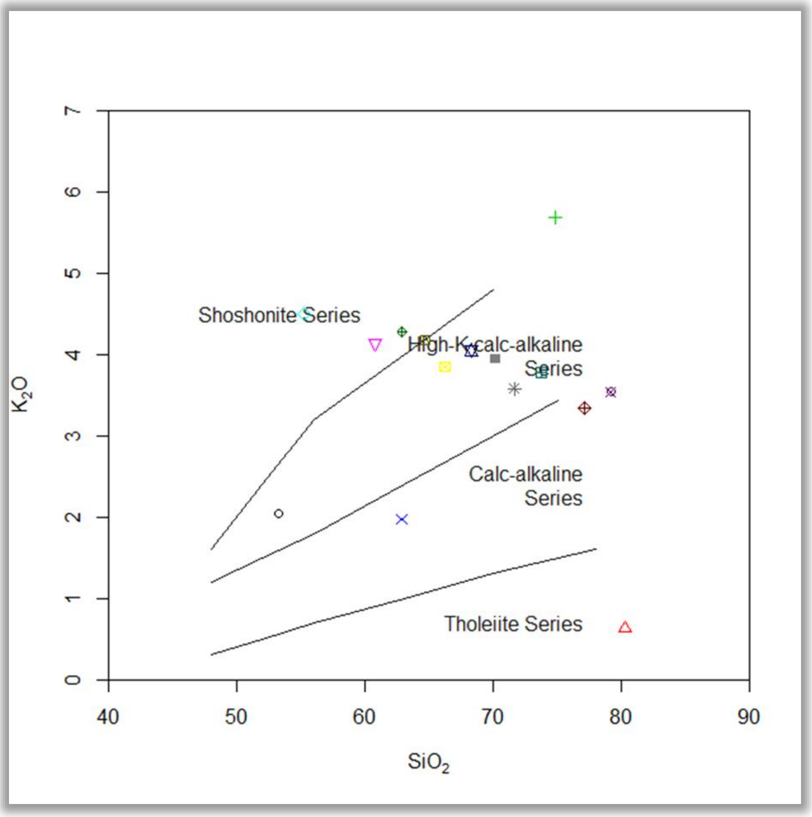


Fig.17. $SiO_2$-$K_2O$ discrimination plot (after Peccerillo and Taylor 1976)

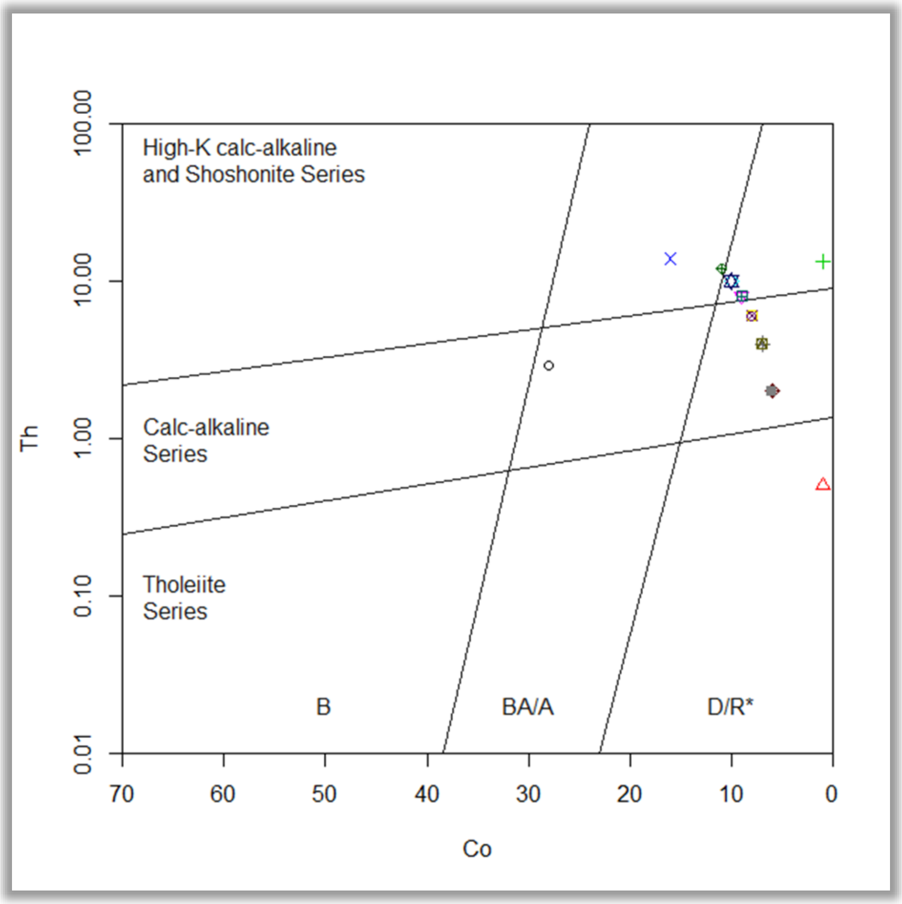


FIG. 18. Co - Th discrimination plot (After Hastie *et al.,* 2007)

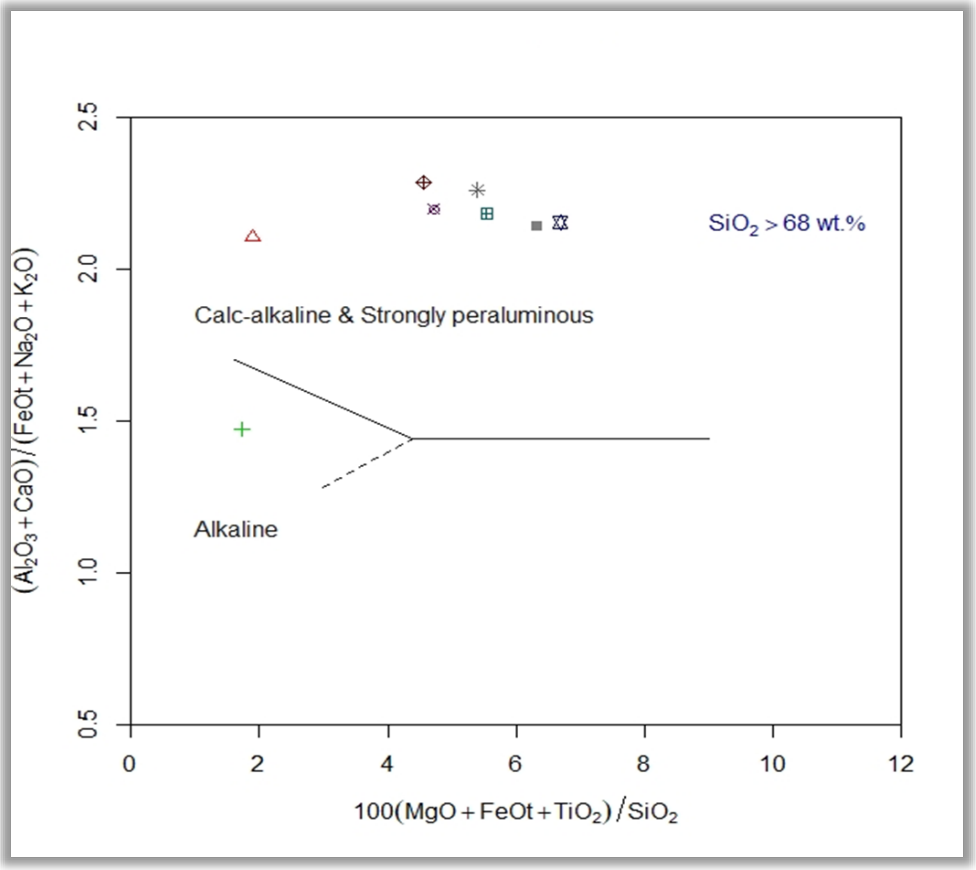


FIG.19. Discrimination plot of $(Al_2O_3+CaO)/(FeOt+Na_2O+K_2O)$ versus $100(MgO+FeOt+TiO_2)/SiO_2$ (fields after Sylvester, 1989)

Index (ASI) exceeding 1 and $Al_2O_3$ surpassing $CaO+Na_2O+K_2O$. Awi sandstones' major oxide geochemistry reveals that $Al_2O_3$ exceeds $CaO+Na_2O+K_2O$, and the ASI is greater than one, confirming the peraluminous nature as depicted in Figures 20, 21, and 22. The Quartz, Alkali feldspar, and Plagioclase feldspar (QAP) diagram for intrusive rocks (Figure 23) shows that Awi sandstones' protolith comprises quartz-rich granitoids. The classification plot of plutonic igneous rocks (Cox, 2013) in Figure 24 indicates that the original rock is granodiorite based on the $Na_2O+K_2O$ vs $SiO_2$ data. Subsequent plots in Figures 25 and 26, provide additional classification based on $Na_2O+K_2O$ versus $SiO_2$ (as per Middlemost, 1985, and 1994). Additionally, Figure 27 displays the R1-R2 classification plot for plutonic igneous rocks (according to De la Roche et al., 1980), confirming that the protolith of Awi sandstone is granodiorite.

**Tectonic Setting**

Sandstones can be formed in various tectonic environments, each with distinct geological processes and environmental conditions. Understanding these environments helps us gain insights into Earth's history and the conditions under which these rocks were deposited. Intermediate and felsic rocks are commonly associated with continental volcanic arcs, continental margins, orogenic belts, and other tectonic settings where magmatic activity contributes to the formation of these rock compositions. Mafic rocks are typically located at divergent plate boundaries, such as mid-ocean ridges. Pearce et al. (1984) utilized Y+Nb versus Rb and Y versus Nb diagrams to construct discrimination plots, which indicated that the Awi sandstones were formed in Volcanic Arc Granite (VAG) and Syn-Collisional Granite (Syn-COLG) settings, suggesting their formation in volcanic arcs or collisional orogeny settings (Figure 28). The discrimination plot created by Pearce and Norry (1979) comparing Zr versus Nb/Zr, utilized in this study, indicates a transformation from subduction to collisional tectonic processes (see Figure 29). Furthermore, Pearce (2008) devised a Nb/Yb - Th/Yb discriminating plot, suggesting a volcanic arc origin for these sandstones (see Figure 30). Moreover, Schandl and Gorton (2002) developed plots comparing Th/Yb versus Ta/Yb and Th versus Ta to

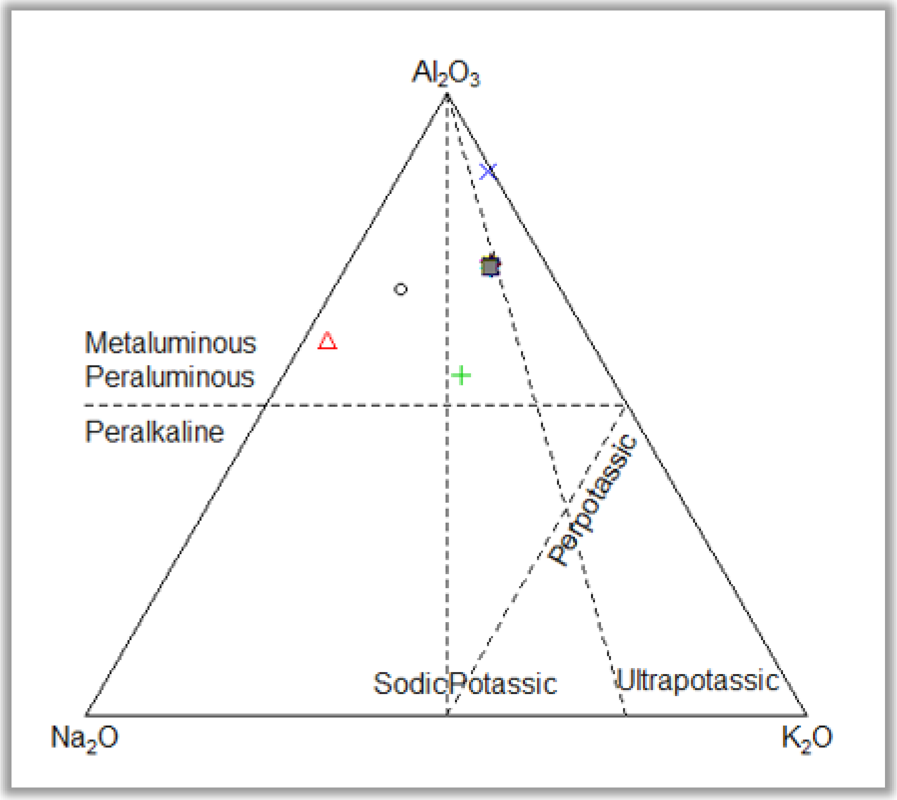


FIG.20. Molar $Na_2O$-$Al_2O_3$-$K_2O$ plot (after Salisu *et al.* 2022).

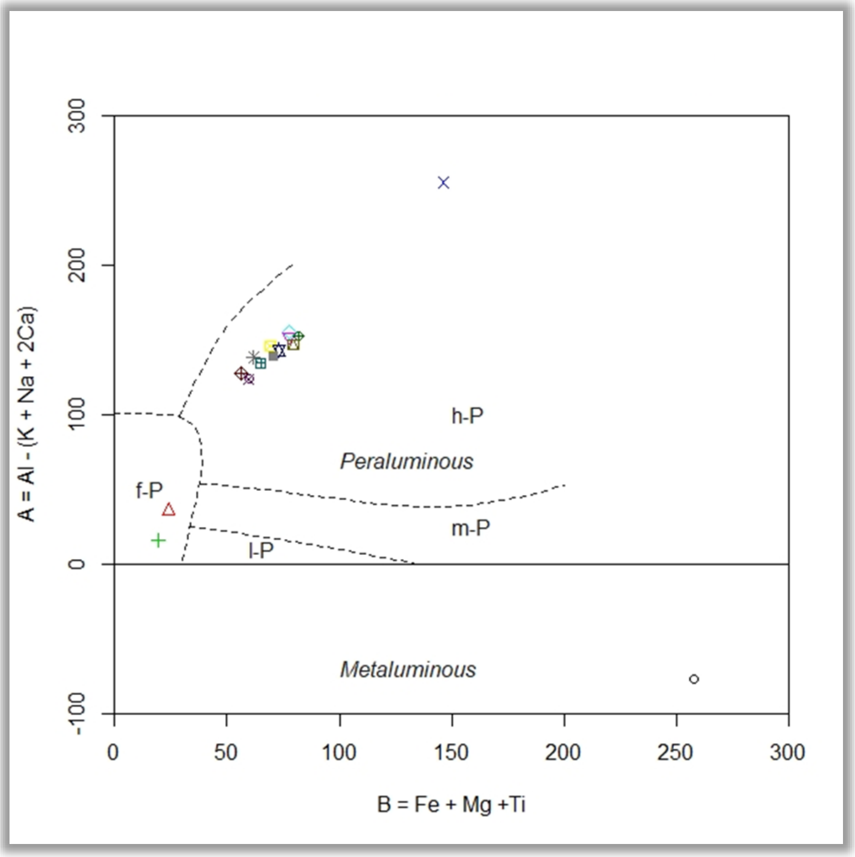


FIG.21. B-A discrimination plot (modified by Villaseca *et al.* 1998). f-P stands for felsic-peraluminous (>1.1), h-P stands for high-peraluminous (1.05-1.1), m-P stands for medium-peraluminous (1.0-1.05), and l-P stands for low-peraluminous (<1.0)

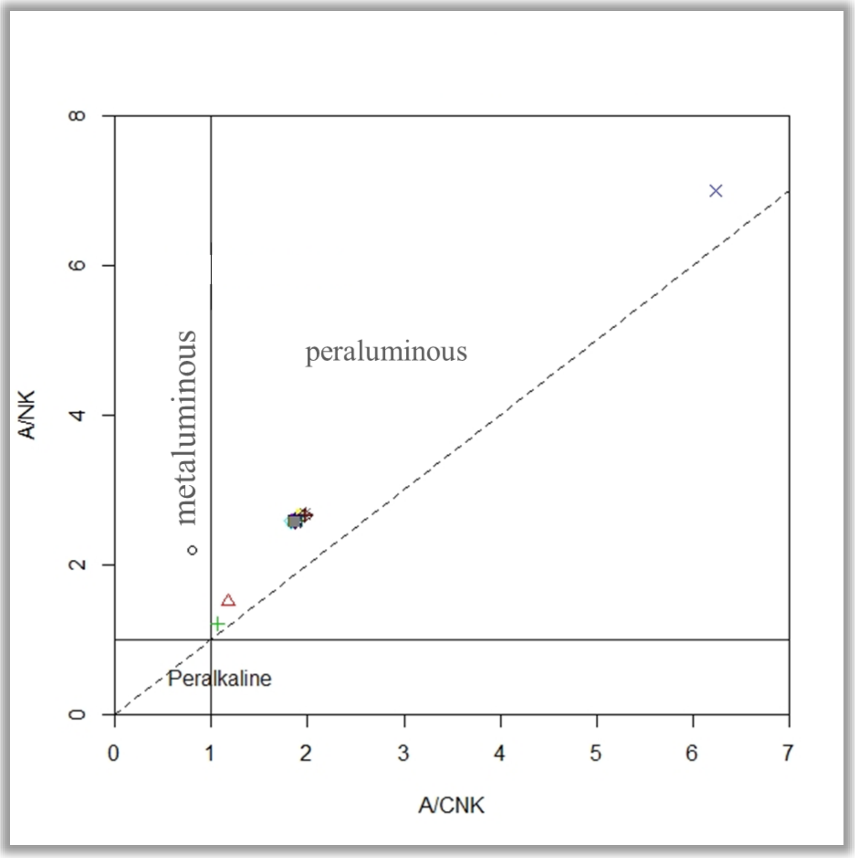


FIG. 22. A/CNK versus A/NK diagram (after Shand 1927)

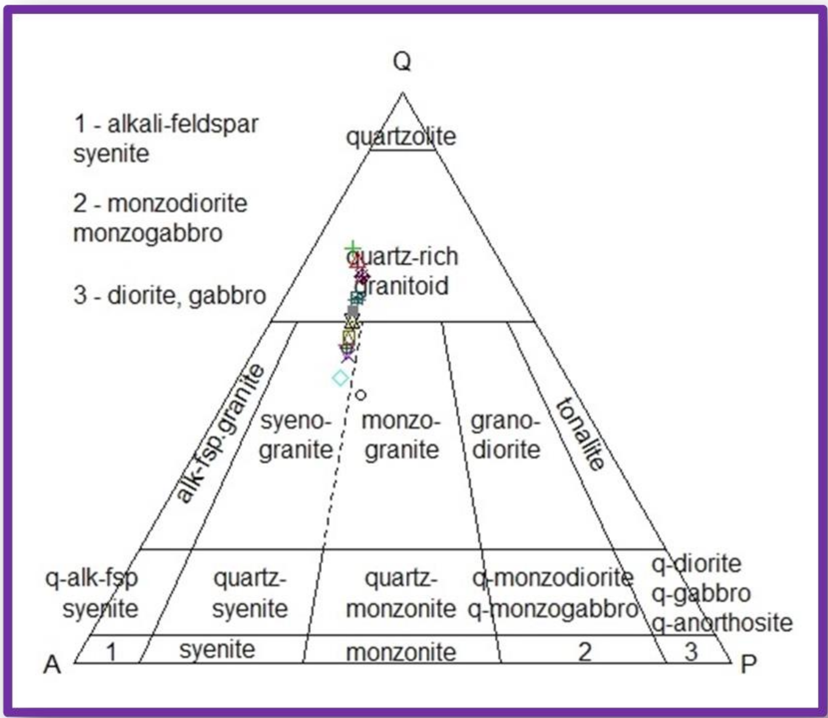


FIG.23. QAP diagram – Si oversaturated for intrusive igneous rocks (After Verma and Rivera-Gómez, 2013)

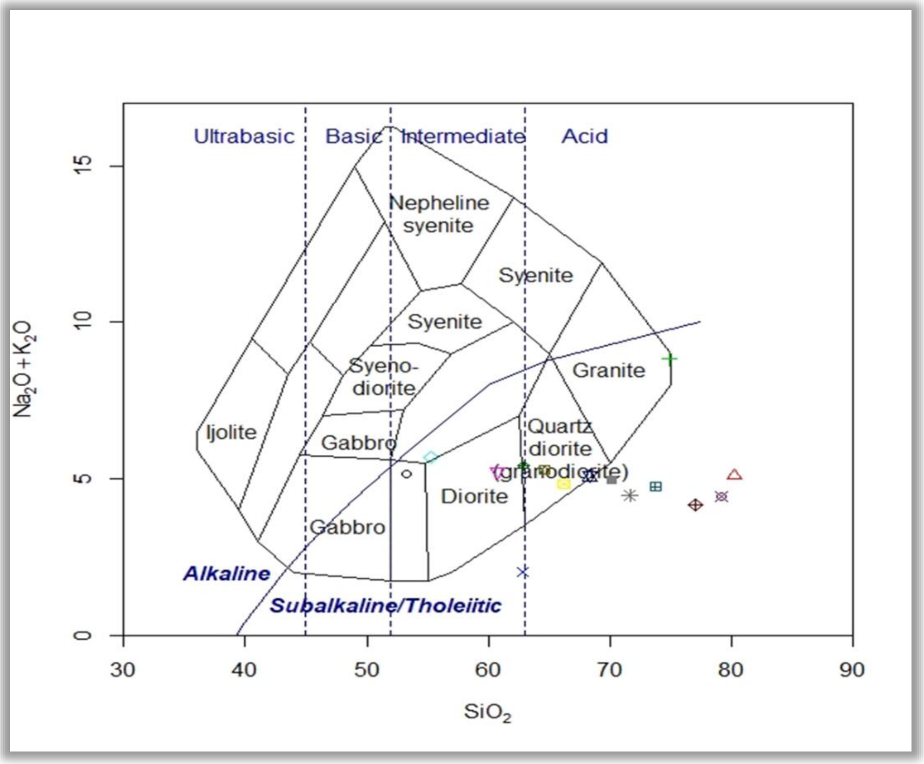


FIG.24. $Na_2O+K_2O$ vs $SiO_2$ classification plot of plutonic igneous rocks (after Cox, 2013)

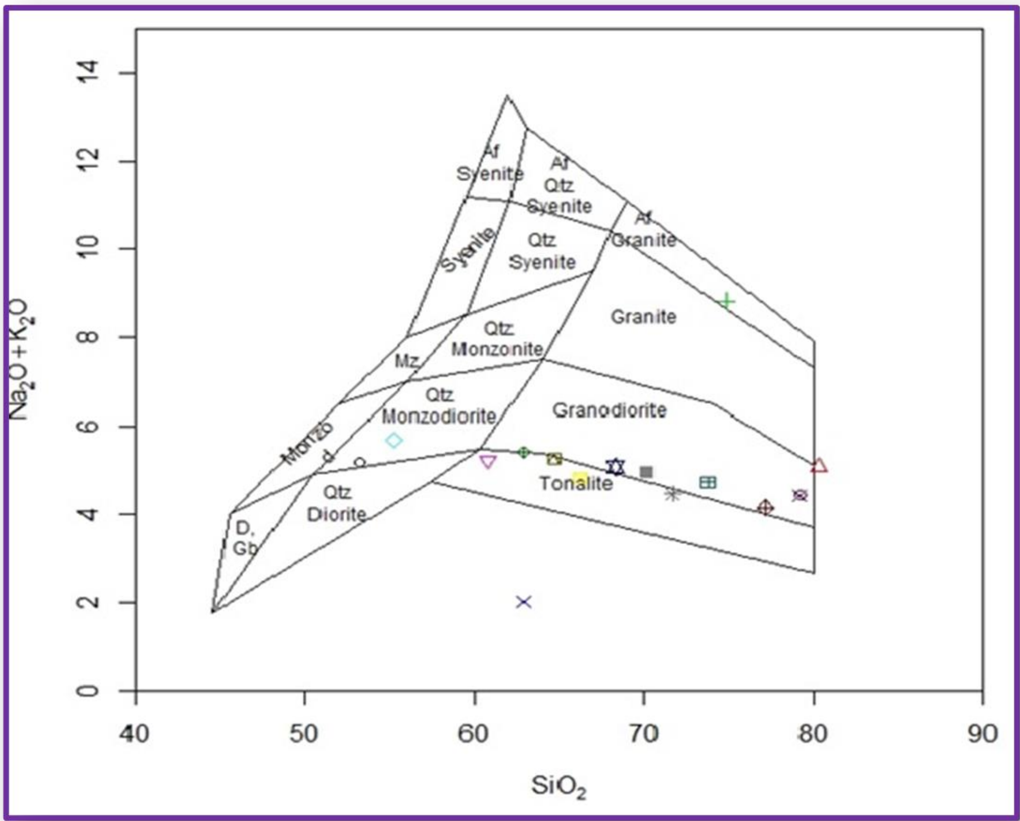


FIG.25. Classification plots of $Na_2O+K_2O$ vs $SiO_2$ (after Middlemost, 1985)

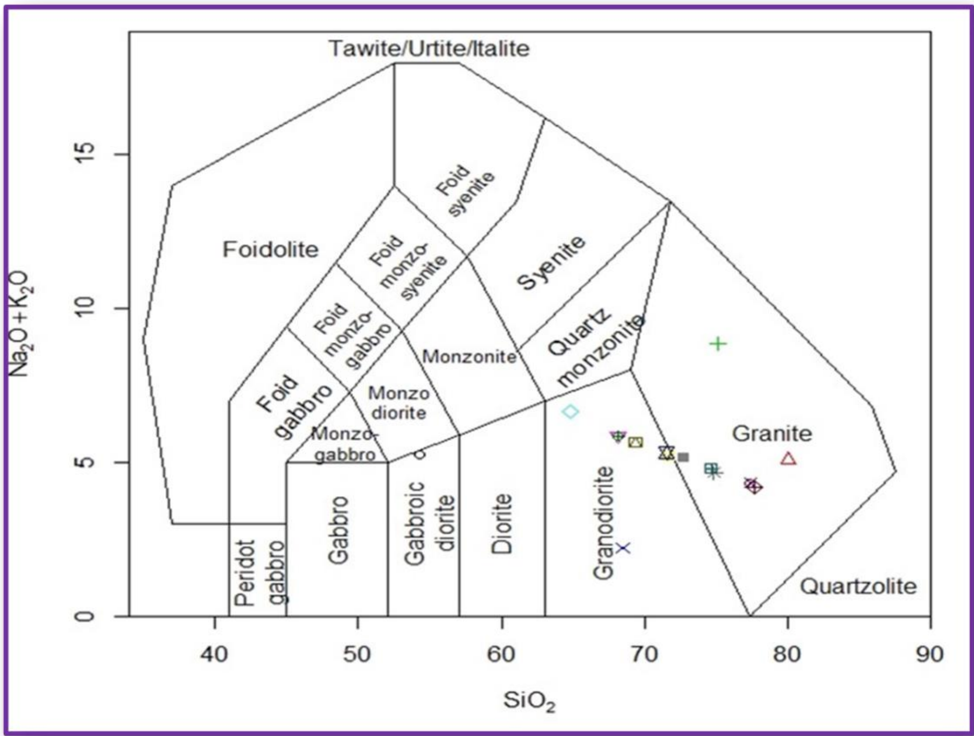


FIG.26. $Na_2O+K_2O$ vs $SiO_2$ classification plot of plutonic igneous rocks (after Middlemost, 1994)

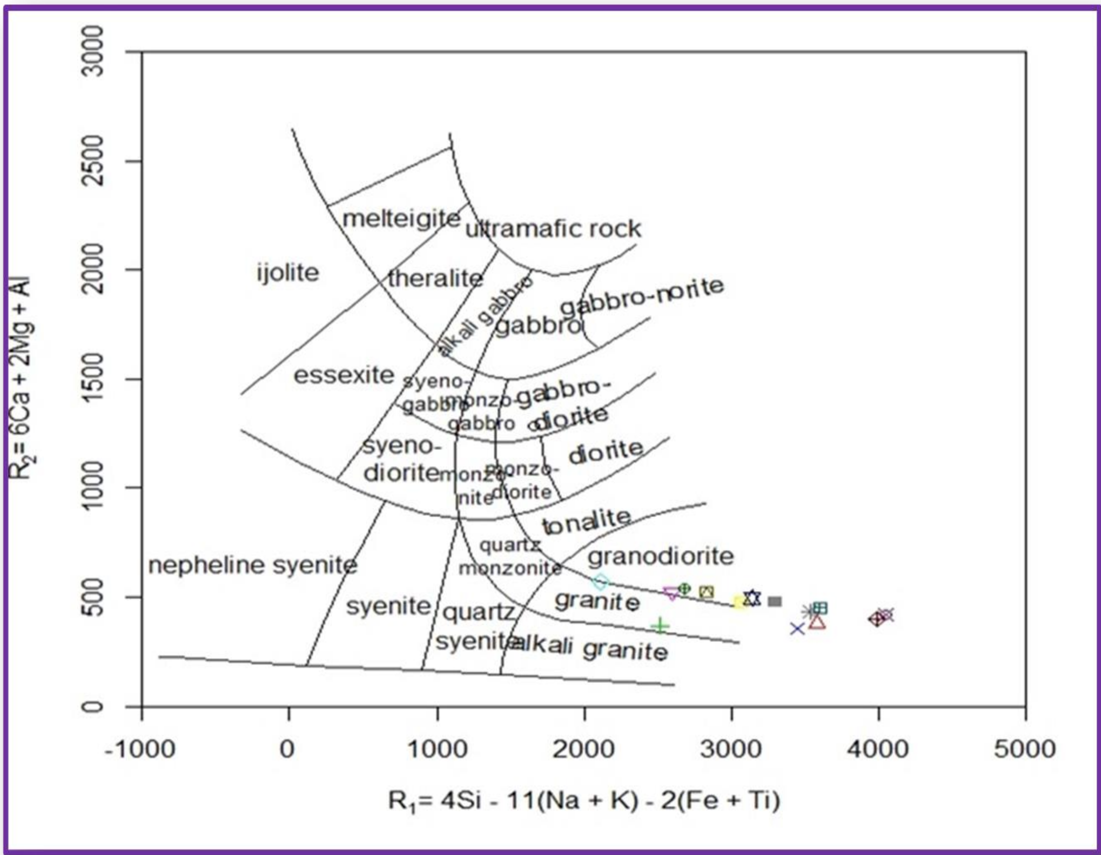


FIG.27. R1-R2 classification plot for plutonic igneous rocks (after De la Roche *et al.,* 1980)

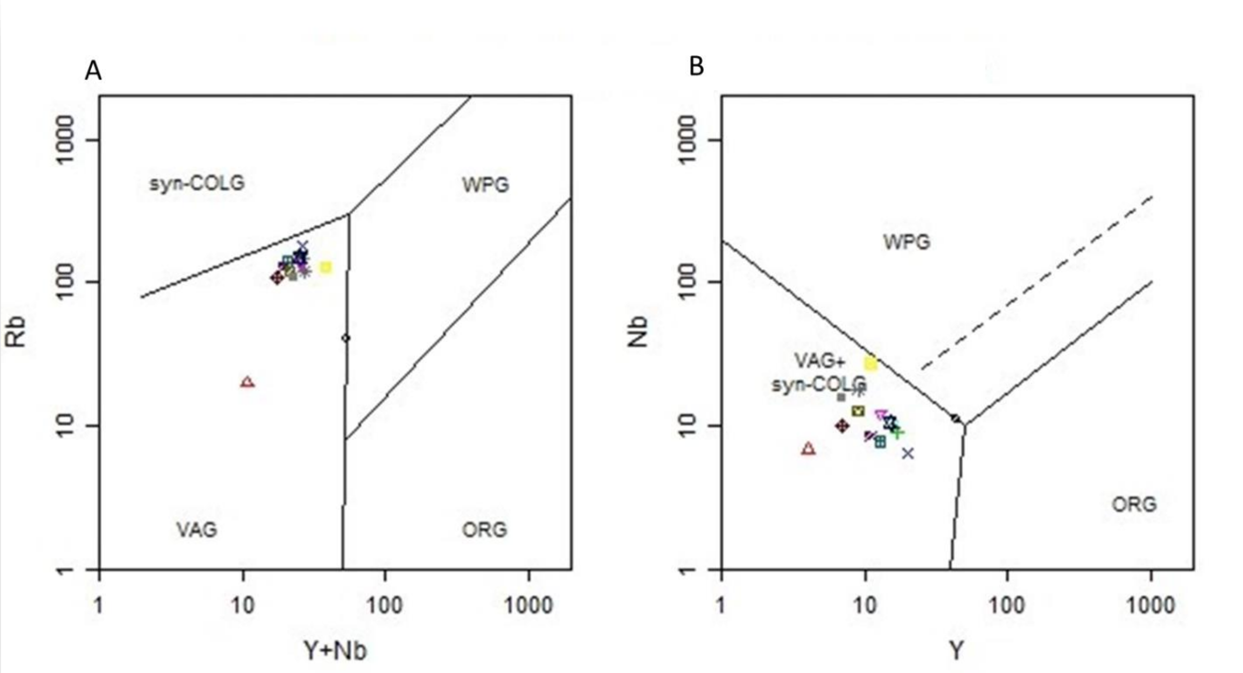


FIG. 28 A. Y+Nb vs Rb and B. Y vs Nb tectonic plot (After Pearce *et al.,* 1984)

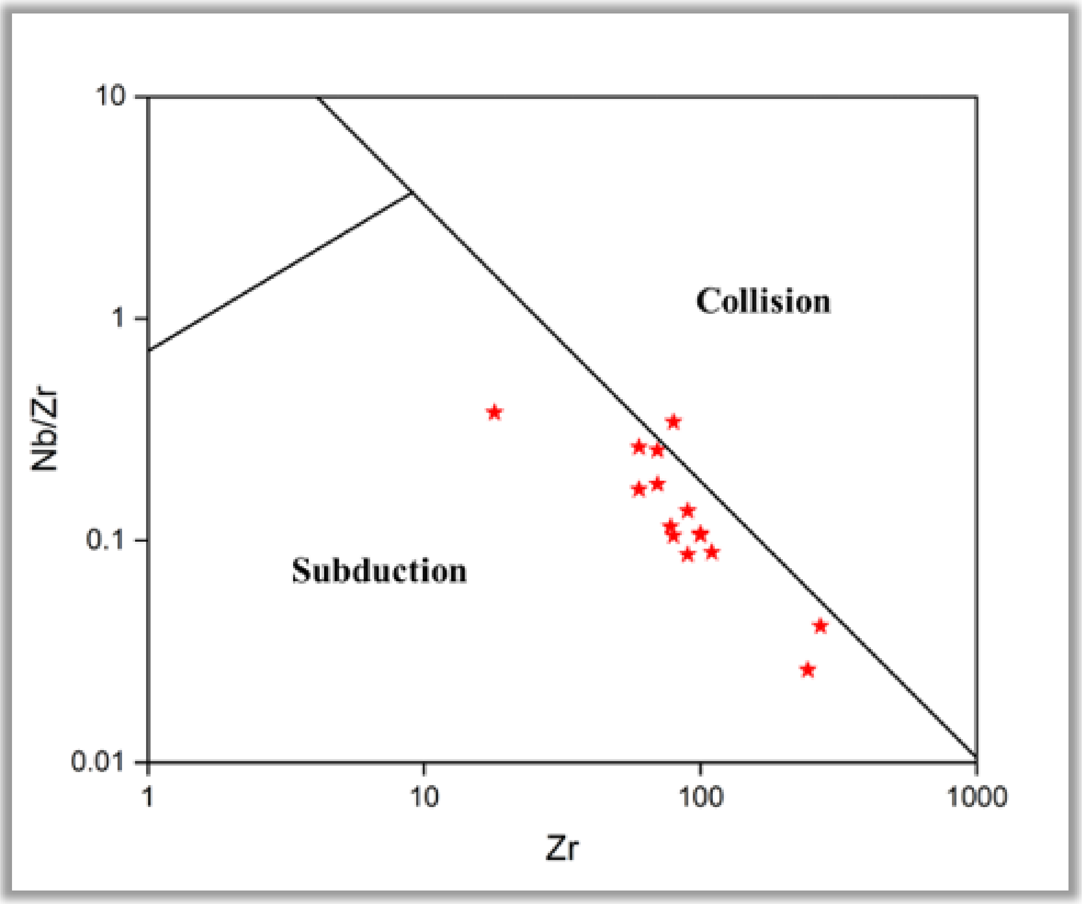


FIG. 29. Discrimination plots of Zr versus Nb/Zr showing subduction and collision regions (Pearce, and Norry, 1979)

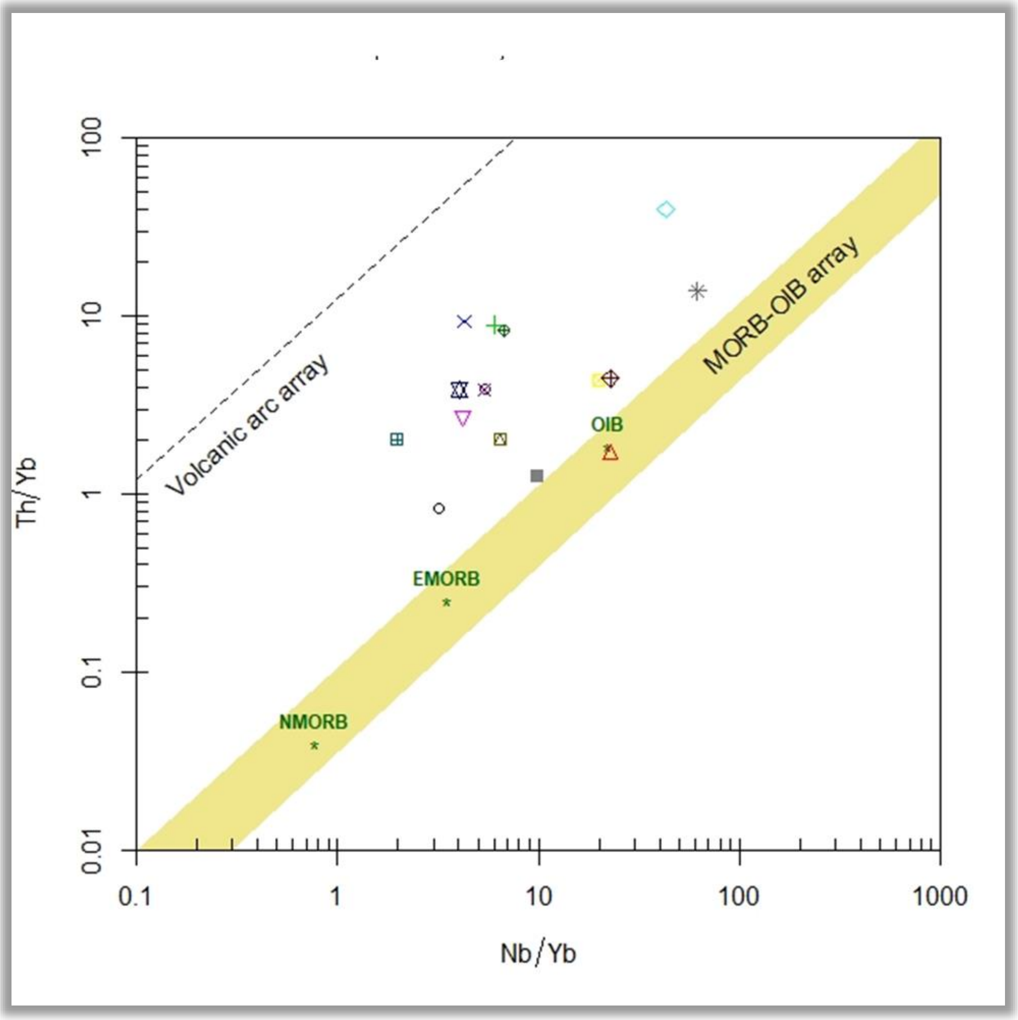


FIG.30. Discrimination plot of Nb/Yb – Th/Yb (fields after Pearce 2008)

classify the tectonic environment of geological materials, indicating that the Awi sandstones were formed in an active continental margin (see Figure 31). Roser and Korsch (1988) also introduced a discrimination diagram based on the log ratio of ($K_2O/Na_2O$) against $SiO_2$ (see Figure 32). This evaluation reveals that the Awi sandstones were mainly derived from a passive margin to an active continental margin setting.

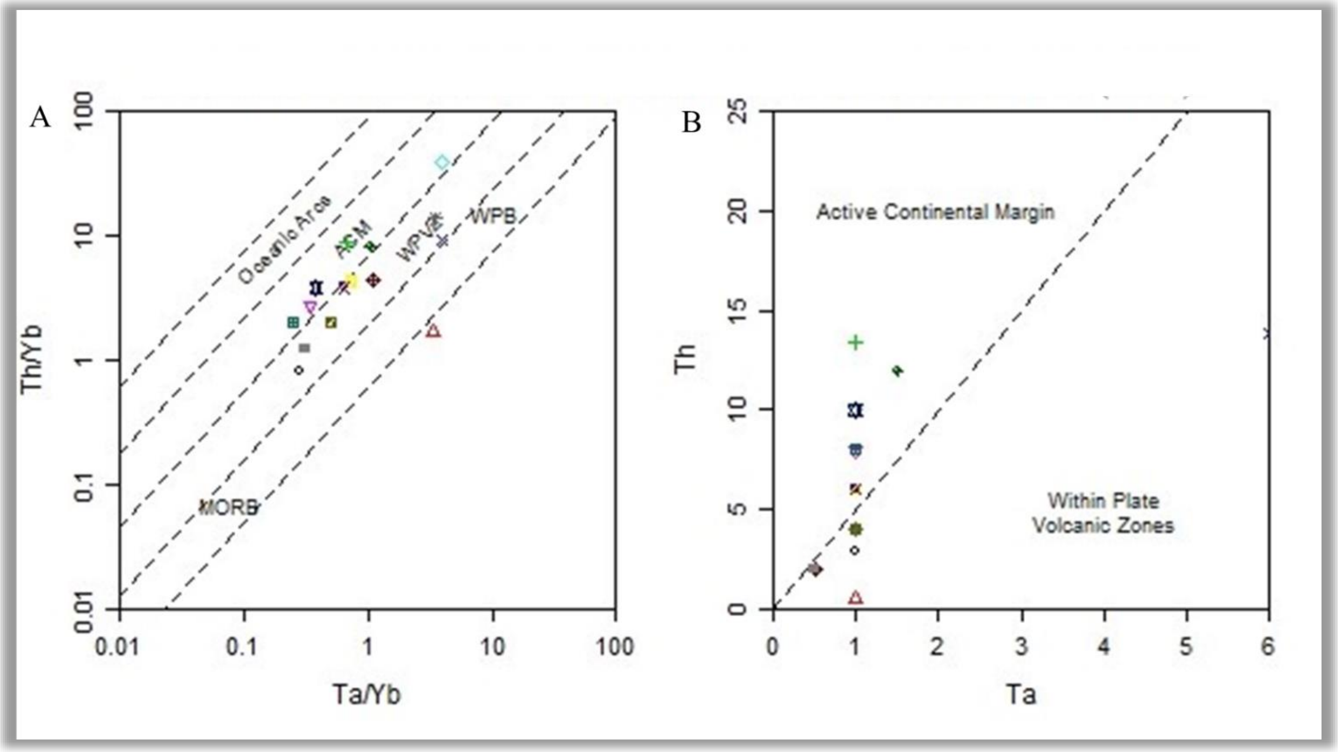


FIG.31A. Th/Yb versus Ta/Yb geotectonic classification of Awi sandstones (After Schandl and Gorton, 2002). B. Th versus Ta geotectonic classification of Awi sandstones (After Schandl and Gorton, 2002)

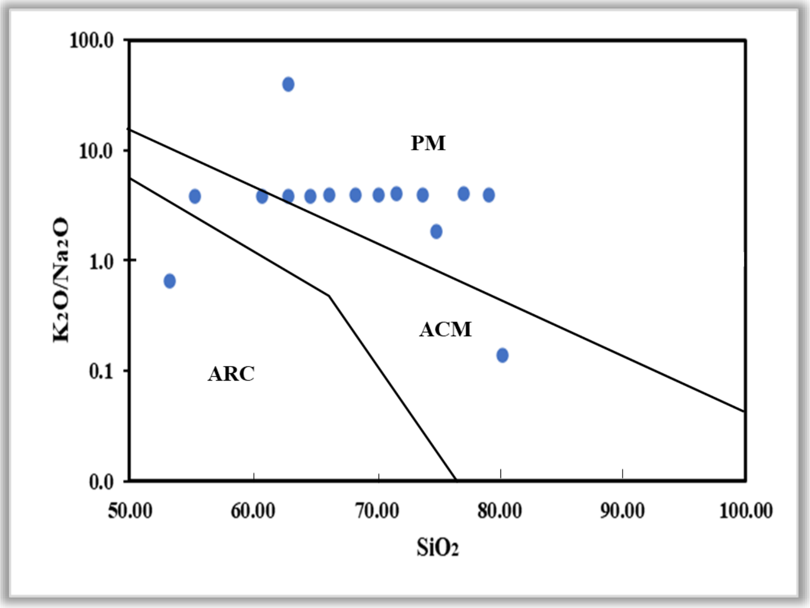


FIG. 32. Discrimination plot of log ratio of ($K_2O/Na_2O$) against $SiO_2$ (Roser and Korsch, 1988)

## SUMMARY

The analysis showed an increase in the presence of Ba, Rb, Sr, Cr, Zn, Ni, Y, and Cu, with the highest enrichment observed in Ba, followed by Rb, Sr, Cr, Zn, Ni, Y, and Cu. Conversely, a decrease was observed in the levels of As, Be, Bi, Cd, Hf, Hg, Mo, Sc, U, and Pb. Additionally, the findings indicated an increase in LREE and a decrease in HREE. According to Hayashi et al. (1997), the $TiO_2$-Zr discrimination plot and Murali et al.'s (1983) major element Discriminant Function diagram suggest that the source rock of Awi sandstones mainly originated from intermediate-felsic igneous provenance. Based on the research conducted by Ross and Bedard (2009), the comparison of Th/Yb versus Zr/Y, as well as the analysis of FeOt/MgO versus $SiO_2$ by Miyashiro (1974), the AFM plot by Irvine and Baragar (1971), the $SiO_2$-$K_2O$ plot by Peccerillo and Taylor (1976), the Co - Th discrimination plot by Hastie et al. (2007), and the $(Al_2O_3+CaO)/(FeOt+Na_2O+K_2O)$ versus $100(MgO+FeOt+TiO_2)/SiO_2$ plot by Sylvester (1989) all point towards the calc-alkaline nature of the Awi sandstone protolith. Additionally, the discrimination plot of $(Al_2O_3+CaO)/(FeOt+Na_2O+K_2O)$ versus $100(MgO+FeOt+TiO_2)/SiO_2$ by Sylvester (1989), the Molar $Na_2O$-$Al_2O_3$-$K_2O$ plot by Salisu et al. (2022), the A/CNK versus A/NK diagram by Shand (1927), and the B-A discrimination plot (modified by Villaseca et al. in 1998) all indicate that the protolith of Awi sandstones is highly peraluminous. The classification plots provided by Cox (1979), Middlemost (1985), and Middlemost (1994), as well as the R1-R2 classification plot by De la Roche et al. (1980), indicate that the predominant protolith for Awi sandstones is granodiorite. According to the tectonic discrimination plots by Pearce et al. (1984), the depositional environment for most of the Awi sandstones is identified as volcanic arc granite (VAG) and syn-collisional granite (syn-COLG). Additionally, the Nb/Zr vs Zr plot suggests that the formation of Awi sandstones took place in a subduction environment. The geotectonic classification plots developed by Schandl and Gorton, (2002), including Th/Yb versus Ta/Yb, Th versus Ta, Th/Hf versus Ta/Hf, and Th/Ta versus Yb, along with the discrimination plot of log ratio of $(K_2O/Na_2O)$ against $SiO_2$ by Roser and Korsch, 1988, indicate that the Awi sandstones' protolith was created in a passive to active continental margin and within plate volcanic environment, suggesting a complex tectonic history involving periods of both extensional and compressional tectonics, as well as significant magmatic and volcanic processes.

## CONCLUSION

The Awi sandstone contains elevated levels of metals such as barium, rubidium, strontium, chromium, zinc, nickel, and yttrium. In terms of potential rare earth elements, it has higher concentrations of light rare earth elements compared to heavy rare earth elements. The Awi sandstone can be linked to two parent rocks: the mafic (amphibolite) and the felsic (granodiorites). The primary parent rock of this sandstone is granodiorite. The tectonic environment in which this sandstone is formed ranges from passive to active continental margins.

## DECLARATIONS

**Ethics approval and consent to participate**

Not applicable

## CONSENT FOR PUBLICATION

Not applicable

## AVAILABILITY OF DATA AND MATERIAL

All data are contained within the manuscript

## COMPETING INTERESTS

All authors declare zero financial or interpersonal conflict of interest that could have influenced the research work or results reported in this research paper.


## FUNDING

This research was not funded by any Governmental or non-governmental agency.

## ACKNOWLEDGEMENTS

The authors would like to acknowledge all the authors for their contribution to ensuring a successful completion of this research work.


## AUTHORS' CONTRIBUTIONS

**Benjamin Odey Omang:** Project conceptualization, design, and supervision. **Temple Okah Arikpo:** Writing, results extraction, analysis, and manuscript first draft. **Ojikutu Latifa Tijani:** Manuscript revision and proofreading

## REFERENCES


Adamu, C. I., Omang, B. O., Oyetade, O. P., Johnson, O., and Nganje, T. N., 2021. Trace and rare earth element geochemistry of the black and grey shales of the Calabar flank, Southeastern Nigeria: constraints on the depositional environment and the degree of metal enrichment. Acta Geochimica, 40, 312-324

Adekoya, J. A., Ola, P. S., and Olabode, S. O., 2014. Possible Bornu Basin hydrocarbon habitat—a review. International Journal of Geosciences, 2014.

Bjørlykke, A., Bingen, B., Billström, K., and Kooijman, E., 2019. The sandstone-hosted Osen lead deposit, Norway: New Pb isotope evidence for sourcing in the underlying granitoid basement. Norwegian Journal of Geology. https://doi.org/10.17850/njg98-4-04

Boboye, O. A., and Okon, E. E., 2014. Sedimentological and geochemical characterization of the Cretaceous strata of Calabar Flank, southeastern Nigeria. Journal of African Earth Sciences, 99, 427–441. https://doi.org/10.1016/j.jafrearsci.2014.04.035

Bogossian, J., Hagemann, S. G., Rodrigues, V. G., Lobato, L. M., and Roberts, M., 2020. Hydrothermal alteration and mineralization in the Faina greenstone belt: Evidence from the Cascavel and Sertão orogenic gold deposits. Ore Geology Reviews, 119, 103293. https://doi.org/10.1016/j.oregeorev.2019.103293

Caracciolo, L., 2020. Sediment generation and sediment routing systems from a quantitative provenance analysis perspective: Review, application and future development. Earth-Science Reviews, 209, 103226.

Cox, K. G. (Ed.)., 2013. The interpretation of igneous rocks. Springer Science & Business Media.

De la Roche H., Leterrier J., Grandclaude P. & Marchal M. 1980. A classification of volcanic and plutonic rocks using $R_1R_2$-diagram and major element analyses – its relationships with current nomenclature. Chemical Geology, 29, 183–210

Edet, J. J., and Nyong, E. E., 1994. Palynostratigraphy of Nkporo Shale exposures (late Campanian-Maastrichtian) on the Calabar Flank, SE Nigeria. Review of palaeobotany and palynology, 80(1-2), 131-147.

Ekpo, B. O., Essien, N., Fubara, E. P., Ibok, U. J., Ukpabio, E. J., and Wehner, H., 2013. Petroleum geochemistry of Cretaceous outcrops from the Calabar Flank, southeastern Nigeria. Marine and Petroleum Geology, 48, 171-185.

Ekpo, B. O., Ibok, U. J., Essien, N., and Wehner, H., 2012. Geochemistry and organic petrography of Cretaceous sediments of the Calabar Flank, southeastern, Nigeria. Marine and Petroleum Geology, 35(1), 252–268. https://doi.org/10.1016/j.marpetgeo.2012.03.010

Ekwok, S. E., Akpan, A. E., Kudamnya, E. A., and Ebong, E. D., 2020. Assessment of groundwater potential using geophysical data: A case study in parts of Cross River State, south-eastern Nigeria. Applied Water Science, 10(6), 144. https://doi.org/10.1007/s13201-020-01224-0

Eldosouky, A. M., Ekwok, S. E., Akpan, A. E., Achadu, O. I. M., Pham, L. T., Abdelrahman, K., ... and Alarifi, S. S., 2022. Delineation of structural lineaments of Southeast Nigeria using high resolution aeromagnetic data. Open Geosciences, 14(1), 331-340.

Fleischer, V. D., 1984. Discovery, geology and genesis of copper—Cobalt mineralisation at Chambishi Southeast prospect, Zambia. Precambrian Research, 25(1–3), 119–133. https://doi.org/10.1016/0301-9268(84)90027-5

Frangipane, G., Pistolato, M., Molinaroli, E., Guerzoni, S., and Tagliapietra, D., 2009. Comparison of loss on ignition and thermal analysis stepwise methods for determination of sedimentary organic matter. Aquatic Conservation: Marine and Freshwater Ecosystems, 19(1), 24-33.

Garzanti, E., 2019. Petrographic classification of sand and sandstone. Earth-Science Reviews, 192, 545–563. https://doi.org/10.1016/j.earscirev.2018.12.014

Goswami, P. K., and Deopa, T., 2018. Petrotectonic setting of the provenance of Lower Siwalik sandstones of the Himalayan foreland basin, southeastern Kumaun Himalaya, India. Island Arc, 27(2), e12242. https://doi.org/10.1111/iar.12242

Gromet, L. P., Haskin, L. A., Korotev, R. L., and Dymek, R. F., 1984. The "North American shale composite": Its compilation, major and trace element characteristics. Geochimica et cosmochimica acta, 48(12), 2469-2482.

Hastie, A. R., Kerr, A. C., Pearce, J. A., and Mitchell, S. F., 2007. Classification of altered volcanic island arc rocks using immobile trace elements: development of the Th–Co discrimination diagram. Journal of petrology, 48(12), 2341-2357.

Hayashi, K. I., Fujisawa, H., Holland, H. D., and Ohmoto, H. (1997). Geochemistry of~ 1.9 Ga sedimentary rocks from northeastern Labrador, Canada. Geochimica et cosmochimica acta, 61(19), 4115-4137.

Hayes, T. S., and Einaudi, M. T., 1986. Genesis of the Spar Lake strata-bound copper-silver deposit, Montana; Part I, Controls inherited from sedimentation and pre-ore diagenesis. Economic Geology, 81(8), 1899-1931.

Heiri, O., Lotter, A. F., and Lemcke, G., 2001. Loss on ignition as a method for estimating organic and carbonate content in sediments: reproducibility and comparability of results. Journal of paleolimnology, 25, 101-110.

Hoogsteen, M. J., Lantinga, E. A., Bakker, E. J., Groot, J. C., and Tittonell, P. A., 2015. Estimating soil organic carbon through loss on ignition: effects of ignition conditions and structural water loss. European Journal of soil science, 66(2), 320-328.

Huston, D. L., Sie, S. H., Suter, G. F., Cooke, D. R., and Both, R. A., 1995. Trace elements in sulfide minerals from eastern Australian volcanic-hosted massive sulfide deposits; Part I, Proton microprobe analyses of pyrite, chalcopyrite, and sphalerite, and Part II, Selenium levels in pyrite; comparison with delta 34 S values and implications for the source of sulfur in volcanogenic hydrothermal systems. Economic Geology, 90(5), 1167-1196.

Irvine, T. N., and Baragar, W. R. A. F., 1971. A guide to the chemical classification of the common volcanic rocks. Canadian journal of earth sciences, 8(5), 523-548.

Le Deit, L., Mangold, N., Forni, O., Cousin, A., Lasue, J., Schröder, S. and Treiman, A. H., 2016. The potassic sedimentary rocks in Gale Crater, Mars, as seen by ChemCam on board Curiosity. Journal of Geophysical Research: Planets, 121(5), 784-804.

Macaulay, E. O., Jonah, U. A., Odama, O. A., Asimay, O., and Edet, O. W., 2016. Stratigraphic Characterization of Parts of the Awi Formation, Calabar Flank, South Eastern Nigeria.

Manning, D. A., 2010. Mineral sources of potassium for plant nutrition. A review. Agronomy for sustainable development, 30, 281-294.

McLennan, S. M., 1981. Trace element geochemistry of sedimentary rocks: implications for the composition and evolution of the continental crust. The Australian National University (Australia).

McLennan, S. M., 2003. Large-ion lithophile element fractionation during the early differentiation of Mars and the composition of the Martian primitive mantle. Meteoritics and Planetary Science, 38(6), 895-904.

Middlemost E.A.K. 1985. Magmas and Magmatic Rocks. Longman, London.

Middlemost E.A.K. 1994. Naming materials in the magma/igneous rock system. Earth-Science Reviews, 37, 215–224

Misra, K., 2012. Understanding mineral deposits. Springer Science and Business Media.

Miyashiro A. 1974. Volcanic rock series in island arcs and active continental margins. American Journal of Science, 274, 321–355

Murali, A. V., Parthasarathy, R., Mahadevan, T. M., and Das, M. S., 1983. Trace element characteristics, REE patterns and partition coefficients of zircons from different geological environments—a case study on Indian zircons. Geochimica et Cosmochimica Acta, 47(11), 2047-2052.

Nton, M. E., 1999. Sedimentology and depositional environment of Awi formation Calabar flank, southeastern Nigeria.

Okunola, O. W., Olatunji, A. S., and Afolabi, A. O., 2023. Geology and Rare Earth Element Geochemistry of Magnesian Granitoids Within Proterozoic Schist Belt of Southwest Nigeria. Materials and Geoenvironment.

Opara, A. I., Onyewuchi, R. A., Selemo, A. O., Onyekuru, S. O., Ubechu, B. O., Emberga, T. T., and Nosiri, O. P. , 2014. Structural and Tectonic Features of Ugep and Environs, Calabar Flank, Southeastern Nigeria: Evidences from aeromagnetic and Landsat-ETM data. Mitteilungen Klosterneuburg, 64, 33-54.

Oyebamiji, A., Falae, P., Zafar, T., Rehman, H. U., and Oguntuase, M., 2023. Genesis of the Qilinchang Pb–Zn deposit, southwestern China: Evidence from mineralogy, trace elements systematics and S–Pb isotopic characteristics of sphalerite. Applied Geochemistry, 148, 105545.

Ogbahon, O. A., and Opeloye, S. A., 2016. Provenance of sandstone on the western flank of Anambra Basin, Southwestern Nigeria. Global Journal of Geological Sciences, 14, 13-21.

Olade, M. A., 2020. Uranium Occurrences and Exploration Potential of Nigeria. Achievers Journal of Scientific Research, 2(2), 1-22.

Odumodu, C. F., 2012. Temperatures and Geothermal gradient fields in the Calabar Flank and parts of the Niger Delta, Nigeria. Petroleum Technology Development Journal, 2(2), 1-15.

Pearce J.A., Harris N.B.W. and Tindle A.G. 1984. Trace element discrimination diagrams for the tectonic interpretation of granitic rocks. Journal of Petrology, 25, 956–983

Pearce, J. A., 2008. Geochemical fingerprinting of oceanic basalts with applications to ophiolite classification and the search for Archean oceanic crust. Lithos, 100(1-4), 14-48.

Pearce, J. A., and Norry, M. J., 1979. Petrogenetic implications of Ti, Zr, Y, and Nb variations in volcanic rocks. Contributions to mineralogy and petrology, 69(1), 33-47.

Peccerillo A. and Taylor S.R. 1976. Geochemistry of Eocene calc-alkaline volcanic rocks from the Kastamonu area, Northern Turkey. Contributions to Mineralogy and Petrology, 58, 63–81

Pe-Piper, G., Triantafyllidis, S., and Piper, D. J., 2008. Geochemical identification of clastic sediment provenance from known sources of similar geology: the Cretaceous Scotian Basin, Canada. Journal of Sedimentary research, 78(9), 595-607.

Plater, A. J., Kirby, J. R., Boyle, J. F., Shaw, T., and Mills, H., 2015. Loss on ignition and organic content. Handbook of Sea-Level Research, 312-330.

Prego, R., Caetano, M., Vale, C., and Marmolejo-Rodríguez, J., 2009. Rare earth elements in sediments of the Vigo Ria, NW Iberian Peninsula. Continental Shelf Research, 29(7), 896-902.

Revan, M. K., Genç, Y., Maslennikov, V. V., Maslennikova, S. P., Large, R. R., and Danyushevsky, L. V., 2014. Mineralogy and trace-element geochemistry of sulfide minerals in hydrothermal chimneys from the Upper-Cretaceous VMS deposits of the eastern Pontide orogenic belt (NE Turkey). Ore Geology Reviews, 63, 129-149.

Rickard, D. T., Willden, M. Y., Marinder, N. E., and Donnelly, T. H., 1979. Studies on the genesis of the Laisvall sandstone lead-zinc deposit, Sweden. Economic Geology, 74(5), 1255-1285.

Roser, B. P., and Korsch, R. J., 1988. Provenance signatures of sandstone-mudstone suites determined using discriminant function analysis of major-element data. Chemical geology, 67(1-2), 119-139.

Ross, P. S., and Bedard, J. H., 2009. Magmatic affinity of modern and ancient subalkaline volcanic rocks determined from trace-element discriminant diagrams. Canadian Journal of Earth Sciences, 46(11), 823-839.

Salısu, S. M., Haruna, A. I., Halılu, M., Abdullahı, F., and Ahmad, T. G., 2022. Morphological Studies and Petrogenetic Relationship of Metatexite Cum Diatexite Migmatites Around Buzaye Area, Bauchi, Nigeria. International Journal of Earth Sciences Knowledge and Applications, 4(3), 380-394.

Samama, J. C., 1976. Comparative review of the genesis of the copper–lead sandstone-type deposits. Cu, Zn, Pb, and Ag Deposits, 1-20.

Schandl, E. S., and Gorton, M. P., 2002. Application of high field strength elements to discriminate tectonic settings in VMS environments. Economic geology, 97(3), 629-642.

Schieber, J., 1991. The origin and economic potential of sandstone-hosted disseminated Pb-Zn mineralization in pyritic shale horizons of the Mid-Proterozoic Newland Formation, Montana, USA. Mineralium Deposita, 26(4). https://doi.org/10.1007/BF00191076

Shand S.J. 1927. Eruptive Rocks. Thomas Murby, London

Shu, Y., Sang, S.-X., Lin, Y.-X., Zhou, X.-Z., Wang, H., and Wang, Z.-L., 2021. The influence of magmatic-hydrothermal activities on porosity and permeability of sandstone reservoirs in the Linxing area, Ordos Basin, Northern China. Journal of Asian Earth Sciences, 213, 104741. https://doi.org/10.1016/j.jseaes.2021.104741

Spears, D. A., 1987. An investigation of metal enrichment in Triassic Sandstones and porewaters below an effluent spreading site, West Midlands, England. Quarterly Journal of Engineering Geology and Hydrogeology, 20(2), 117-129.

Sun, L., Gui, H., and Chen, S., 2013. Geochemistry of sandstones from the Neoproterozoic Jinshanzhai Formation in northern Anhui Province, China: Provenance, weathering and tectonic setting. Chinese Journal of Geochemistry, 32, 95-103

Sylvester, P. J., 1989. Post-collisional alkaline granites. The Journal of Geology, 97(3), 261-280.

Taylor, S. R., and McLennan, S. M., 1983. Geochemistry of early Proterozoic sedimentary rocks and the Archean/Proterozoic boundary. Geological Society of America Memoirs, 161, 119-132.

Tornos, F., 2006. sEnvironment of formation and styles of volcanogenic massive sulfides: The Iberian Pyrite Belt. Ore Geology Reviews, 28(3), 259-307.

Verma, S. P., and Rivera-Gómez, M. A., 2013. Computer programs for the classification and nomenclature of igneous rocks. Episodes, 36(2), 115-124.

Villaseca, C., Barbero, L., and Rogers, G., 1998. Crustal origin of Hercynian peraluminous granitic batholiths of Central Spain: petrological, geochemical and isotopic (Sr, Nd) constraints. Lithos, 43(2), 55-79.

Wang, Q., Liang, X., Wang, W., Niu, Q., Zhuo, J., Su, X., Zhou, G., Zhao, L., Li, P., Yuan, W., Chang, J., Ji, Z., and Su, A., 2022. Mineral Composition and Full-Scale Pore Structure of Qianjiadian Sandstone-Type Uranium Deposits: Application for In Situ Leaching Mining. Geofluids, 2022, 1–15. https://doi.org/10.1155/2022/2860737

Weltje, G. J., and von Eynatten, H., 2004. Quantitative provenance analysis of sediments: review and outlook. Sedimentary Geology, 171(1-4), 1-11.

Weng, Z., Jowitt, S. M., Mudd, G. M., and Haque, N., 2015. A detailed assessment of global rare earth element resources: opportunities and challenges. Economic Geology, 110(8), 1925-1952.

Zaid, S. M., 2015. Geochemistry of sandstones from the Pliocene Gabir Formation, north Marsa Alam, Red Sea, Egypt: implication for provenance, weathering and tectonic setting. Journal of African Earth Sciences, 102, 1-17.